Rest-frame UV properties of luminous strong gravitationally lensed Lyα emitters from the BELLS GALLERY Survey

R. Marques-Chaves [1,2,3]★ I. Pérez-Fournon,[2,3] Y. Shu [4] L. Colina,[1,5] A. Bolton,[6]
J. Álvarez-Márquez,[1] J. Brownstein,[7] M. Cornachione,[8] S. Geier,[2,9]
C. Jiménez-Ángel,[2,3] T. Kojima,[10,11] S. Mao,[12,13] A. Montero-Dorta,[14] M. Oguri,[11,15]
M. Ouchi,[10,15] F. Poidevin,[2,3] R. Shirley [2,3] and Z. Zheng[7]

[1]*Centro de Astrobiología (CSIC-INTA), Carretera de Ajalvir, E-28850 Torrejón de Ardoz, Madrid, Spain*
[2]*Instituto de Astrofísica de Canarias, C/Vía Láctea, s/n, E-38205 San Cristóbal de La Laguna, Tenerife, Spain*
[3]*Dpto. Astrofísica, Universidad de La Laguna, E-38206 San Cristóbal de La Laguna, Tenerife, Spain*
[4]*Institute of Astronomy, University of Cambridge, Madingley Road, Cambridge CB3 0HA, UK*
[5]*Cosmic Dawn Center (DAWN)*
[6]*NSF's National Optical-Infrared Astronomy Research Laboratory, 950 North Cherry Ave, Tucson, AZ 85719, USA*
[7]*Department of Physics and Astronomy, University of Utah, 115 S. 1400 E., Salt Lake City, UT 84112, USA*
[8]*Department of Physics, United States Naval Academy, 572C Holloway Road, Annapolis, MD 21402, USA*
[9]*GRANTECAN, Cuesta de San José s/n, E-38712 Breña Baja, La Palma, Spain*
[10]*Institute for Cosmic Ray Research, The University of Tokyo, 5-1-5 Kashiwanoha, Kashiwa, Chiba 277-8582, Japan*
[11]*Department of Physics, The University of Tokyo, 7-3-1 Hongo, Bunkyo-ku, Tokyo 113-0033, Japan*
[12]*Physics Department and Tsinghua Center for Astrophysics, Tsinghua University, Beijing 100084, China*
[13]*National Astronomical Observatories, Chinese Academy of Sciences, 20 Datun Road, Beijing 100101, China*
[14]*Departamento de Física Matemática, Instituto de Física, Universidade de São Paulo, Rua do Matão 1371, CEP 05508-090 São Paulo, Brazil*
[15]*Kavli Institute for the Physics and Mathematics of the Universe, University of Tokyo, Kashiwa, Chiba 277-8583, Japan*

ABSTRACT

We present deep rest-frame UV spectroscopic observations using the Gran Telescopio Canarias of six gravitationally lensed Lyα emitters (LAEs) at $2.36 < z < 2.82$ selected from the BELLS GALLERY survey. By taking the magnifications into account, we show that LAEs can be as luminous as $L_{Ly\alpha} \simeq 30 \times 10^{42}\,\mathrm{erg\,s^{-1}}$ and $M_{UV} \simeq -23\,(\mathrm{AB})$ without invoking an AGN component, in contrast with previous findings. We measure Lyα rest-frame equivalent widths, $EW_0\,(Ly\alpha)$, ranging from 16 to 50 Å and Lyα escape fractions, $f_{esc}\,(Ly\alpha)$, from 10 per cent to 40 per cent. Large $EW_0\,(Ly\alpha)$ and $f_{esc}\,(Ly\alpha)$ are found predominantly in LAEs showing weak low-ionization ISM absorption ($EW_0 \lesssim 1$ Å) and narrow Lyα profiles ($\lesssim 300\,\mathrm{km\,s^{-1}}$ FWHM) with their peak close ($\lesssim 80\,\mathrm{km\,s^{-1}}$) to their systemic redshifts, suggestive of less scatter from low H I column densities that favours the escape of Lyα photons. We infer stellar metallicities of $Z/Z_\odot \simeq 0.2$ in almost all LAEs by comparing the P-Cygni profiles of the wind lines N V1240 Å and C IV1549 Å with those from stellar synthesis models. We also find a trend between M_{UV} and the velocity offset of ISM absorption lines, such as the most luminous LAEs experience stronger outflows. The most luminous LAEs show star formation rates up to $\simeq 180\,\mathrm{M_\odot\,yr^{-1}}$, yet they appear relatively blue ($\beta_{UV} \simeq -1.8$ to -2.0) showing evidence of little dust attenuation [$E(B - V) = 0.10$–0.14]. These luminous LAEs may be particular cases of young starburst galaxies that have had no time to form large amounts of dust. If so, they are ideal laboratories to study the early phase of massive star formation, stellar and dust mass growth, and chemical enrichment histories of starburst galaxies at high-z.

Key words: gravitational lensing: strong – galaxies: formation – galaxies: high-redshift.

★ E-mail: ruijmcoelho@gmail.com

1 INTRODUCTION

Lyα emitters (LAEs) are young star-forming galaxies that emit Lyα radiation from the photoionization of neutral hydrogen by young hot stars. LAEs have been detected mainly with narrow-band imaging of their Lyα emission line (typically defined by rest-frame equivalent widths $EW_0 > 20$ Å; e.g. Ajiki et al. 2003; Ouchi et al. 2005, 2008).

Multiwavelength follow-up imaging and spectroscopy have revealed that typical (L^*) LAEs have relatively low stellar masses (M_* $\simeq 10^7$–10^9 M$_\odot$; e.g. Gawiser et al. 2007; Ono et al. 2010a, b; Guaita et al. 2011; Kusakabe et al. 2018), show modest star formation rates (SFR ~ 10 M$_\odot$ yr^{-1}, e.g. Nakajima et al. 2012; Sobral et al. 2018a), and present, on average, low gas-phase metallicity (e.g. Finkelstein et al. 2011; Nakajima et al. 2012, 2013; Amorín et al. 2017; Kojima et al. 2017). They show very compact and clumpy morphologies (effective radius $r_{\rm eff} \simeq 1$ kpc) with little to no evolution with redshift (e.g. Bond et al. 2009; Taniguchi et al. 2009; Bond et al. 2012; Hernán-Caballero et al. 2017; Cornachione et al. 2018; Paulino-Afonso et al. 2018; Shibuya et al. 2019).

Since LAEs have low stellar mass and present strong Lyα emission, which is indicative of a young starburst, they have been used as probes of the very first galaxies, holding important clues to the formation and evolution of galaxies at the time when the Universe was still young (e.g. Finkelstein et al. 2013; Bouwens et al. 2015; Zitrin et al. 2015; Laporte et al. 2017; Hashimoto et al. 2018; Matthee et al. 2018; Hashimoto et al. 2019).

Although LAEs may share several of its physical properties with the Lyman break galaxy (LBG) population (e.g. Shapley et al. 2003; Verhamme et al. 2008; Schaerer, de Barros & Stark 2011; Du et al. 2018; Santos et al. 2019), in particular those showing strong Lyα emission, narrow-band selected LAEs are typically fainter in the ultraviolet (UV) continuum than LBGs, given the nature of the search strategy. Because of that, the characterization of the physical properties of LAEs has been possible using mainly stacking techniques over large samples of individual spectra or images (e.g. Ono et al. 2010a; Wardlow et al. 2014; Momose et al. 2016; Nakajima et al. 2018a).

Another way to study in detail these high-redshift galaxies is to use the natural magnification and amplification produced by gravitational lensing. The Baryon Oscillation Spectroscopic Survey Emission-Line Lens Survey for the GALaxy-Lyα EmitteR sYstems (BELLS GALLERY; Shu et al. 2016b) led to the discovery of 187 galaxy-scale strong gravitational lens candidates with LAEs at $2 < z < 3$ as background sources. Among these, 21 of the highest quality candidates were observed with *Hubble Space Telescope* (*HST*) confirming the lensing nature (Shu et al. 2016c) and providing a detailed characterization of their rest-frame UV continuum surface brightness profiles and substructure down to scales of 100 pc (Cornachione et al. 2018; Ritondale et al. 2019).

The BELLS GALLERY project presented in Shu et al. (2016b) is the first and still unique dedicated survey aimed to search for strong gravitational lensed systems with LAEs as background sources. By taking advantage of the boost on the observable flux and the improved spatial resolution provided by gravitational lensing, many aspects of the physical properties of LAEs can be studied in much more detail than in non-lensed systems. In this paper, we present optical spectroscopic and imaging follow-up observations with the Gran Telescopio Canarias (GTC) and the William Herschel Telescope (WHT) of six gravitationally lensed LAEs from the BELLS GALLERY survey.

The paper is structured as follows. In Section 2, we describe our sample and the spectroscopic and imaging observations. In Section 3, we present the lens model of BG1501+3042, a new confirmed lensed LAE. The analysis of imaging and spectroscopic data are described in Sections 4 and 5, respectively. Finally, in Sections 6 and 7 we discuss our results and summarize our main findings. Throughout this work, we adopted a concordance cosmology with $\Omega_{\rm m} = 0.274$, $\Omega_\Lambda = 0.726$, and $H_0 = 70$ km s^{-1} Mpc^{-1}. All magnitudes are given in the AB system.

2 SAMPLE AND OBSERVATIONS

2.1 Sample selection

From the *HST* sample analysed in Shu et al. (2016c), we restricted the GTC spectroscopic follow-up observations to four LAEs showing large *HST* V-band flux densities and large image separations. This allows us to obtain high signal-to-noise ratio (S/N) spectra, avoiding at the same time large flux contamination from the foreground lens galaxies. These are SDSS J020121.39+322829.6, SDSS J074249.68+334148.9, SDSS J075523.52+344539.5, and SDSS J091859.21+510452.5 (hereafter BG0201+3228, BG0742+3341, BG0755+3445, and BG0918+5104, where 'BG' stands for BELLS GALLERY).

The LAEs BG0201+3228, BG0742+3341, and BG0918+5104 are magnified by factors of $\mu = 15 \pm 3$, 16 ± 3, and 18 ± 3, respectively (Shu et al. 2016c), and show similar lensed morphologies, with bright extended arcs and relatively compact counter-images on the other side of the lens in a *cusp* configuration. BG0755+3445 shows an Einstein-cross-like configuration composed of four bright lensed images in the image plane (A to D in Fig. 1), all of them observed with the GTC, and is magnified by $\mu = 14 \pm 2$.

We also re-observed BG1429+1202, discussed already in Marques-Chaves et al. (2017) (see also Rigby et al. 2018b; Chisholm et al. 2019), this time with higher spectral resolution and deeper imaging. This system comprises four images in the observer plane with a total magnification of 8.8 (Marques-Chaves et al. 2017), forming a *fold* configuration: a bright lensed image pair, A and B (with a separation of $\approx$1.5 arcsec), and two fainter images, C and D (see Fig. 1). The GTC long slit was positioned so as to encompass the two brightest lensed images A and B.

In addition, we observed another promising lensed system candidate from the parent sample composed of 166 BELLS GALLERY of Shu et al. (2016b). SDSS J150114.60+304230.8, hereafter BG1501+3042, shows bluish (i.e. $r - i \simeq 0$) features $\approx$3.7 arcsec SE from the luminous red galaxy (LRG) at $z_{\rm lens} = 0.638$, and its BOSS spectrum (Plate-MJD-Fiber: 3875–55364–935; Blanton et al. 2017) shows an emission line at $\simeq$ 4438 Å, likely Lyα emission at $z \simeq 2.65$.

2.2 Spectroscopic data

The spectroscopic survey was conducted with the Optical System for Imaging and low-Intermediate Resolution Integrated Spectroscopy instrument (OSIRIS)[1] mounted at the GTC, at the Observatorio del Roque de los Muchachos. The observations were obtained in service mode over 10 different nights, between 2017 January 26 and 2018 February 16, as part of the GTC programs GTC47-16B, GTC67-17A, and GTCMULTIPLE2F-17B (PI: R. Marques-Chaves). The seeing conditions ranged between 0.7 and 1.1 arcsec. We used 1.2 and 1.0 arcsec-wide long slits oriented to cover the
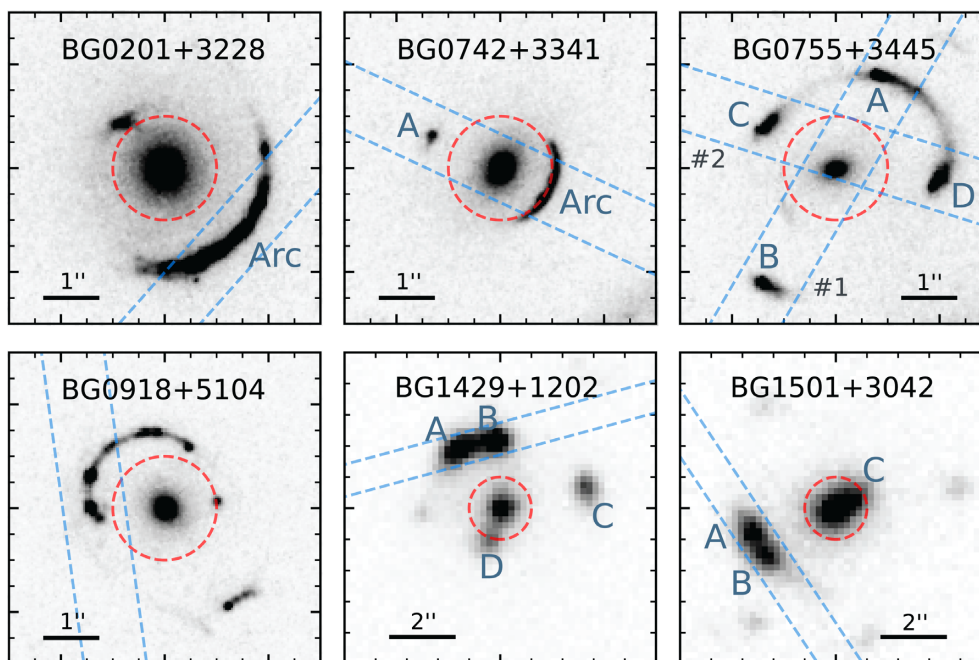
---

[1] http://www.gtc.iac.es/instruments/osiris/

Figure 1. Cutouts of the six lensed LAEs analysed in this work from *F*606*W* images obtained by *HST* (BG0201+3228, BG0742+3341, BG0755+3445, and BG0918+5104) and GTC (BG1429+1202 and BG1501+3042). The orientations of the GTC/OSIRIS long slit are marked with blue dashed lines, as well as the position of the spectroscopic 1 arcsec-radius BOSS fibre (red dashed circles). The images are centred on the LRGs and oriented such that north is up and east is to the left.

regions of maximum emission in order to maximize the S/N (see Fig. 1). Depending on each LAE (details of these observations are listed in Table 1), the total integration time ranged between 2100 and 7200 s. The spectra were obtained with the R2500V, R2500R, R2000B, and R1000B grisms, providing a spectral coverage of 3630–7685 Å. The data were reduced with standard IRAF tasks. 1D spectra were extracted and corrected for the instrumental response using spectroscopic observations of several standard stars. Atmospheric extinction and airmass have been taken into account.

2.3 Imaging data

We carried out imaging observations with the GTC and WHT of five of these lensed LAEs. The lensed LAEs were observed between 2015 April 24 and 2017 May 22 with the Sloan *g*, *r*, and *i* broad-band filters. The GTC images were obtained with the OSIRIS instrument, with a field of view of 7.8 arcmin × 8.5 arcmin and a plate scale of 0.254 arcsec pix^{-1}. WHT data were obtained using the Auxiliary-port Camera[2] (ACAM: Benn, Dee & Agócs 2008) with a circular field of view of 8 arcmin diameter and a plate scale of 0.254 arcsec pix^{-1}. The total integration time ranged between 420 and 900 s for each band, split into several individual exposures (for cosmic rays rejection), under sub-arcsec seeing conditions (≈0.7−0.9 arcsec FWHM).

For all imaging observations, each frame was reduced individually following standard reduction procedures in IRAF. These include subtraction of the bias and further correction of the flat-field using, when possible, skyflats from low crowded fields. The registration and combination were done using SCAMP (Bertin 2006) and SWARP (Bertin 2010), and the astrometry was improved using *Gaia* stars

[2]http://www.ing.iac.es/astronomy/instruments/acam/

from the first data release DR1 (Gaia Collaboration 2016), yielding a typical rms of ≃ 0.07 arcsec. Finally, the images were flux-calibrated against SDSS (Data Release 9 catalogue; Ahn et al. 2012) using stars in the field of view. The GTC images reach 3σ point source magnitude limits of 25.9, 25.8, and 25.3 mag in the *g*, *r*, and *i* filters, respectively. The WHT imaging data reach a depth of 25.5 and 23.3 mag in the *g* and *i* filters, respectively.

In addition, we have used archival *R* and *I* wide-field images of BG0918+5104 from MEGACAM on the Canada–France–Hawaii Telescope (CFHT), processed and stacked using the MegaPipe image staking pipeline (Gwyn 2008), and downloaded from the Canadian Astronomy Data Centre. Total exposure times are 3200 and 2560 s in *R* and *I* bands, with an average seeing of 0.85 and 0.55 arcsec FWHM, and a 3σ limiting magnitude of 26.7 and 25.7 (point source), respectively.

3 BG1501+3042: CONFIRMATION OF A NEW LENSED LYα EMITTER

BG1501+3042 was initially selected by Shu et al. (2016b) as a lensed LAE candidate by the detection of an asymmetric emission line at ≃4435 Å (likely Lyα emission at *z* = 2.649) in the BOSS spectrum of the *z* = 0.638 LRG SDSS J150114.60+304230.8. The GTC broad-band images (see Fig. 2) show two bright components at ≃ 3.7 arcsec SE from the LRG (marked as 'A' and 'B'), and another one ('C') partially blended with the LRG ('G'). The GTC spectrum encompassing the bright components 'A' and 'B' shows a bright Lyα emission line at *z* = 2.649 (see Fig. 2), consistent with the emission line found in the BOSS spectrum of the LRG, that arises from 'C'. Therefore, BG1501+3042 comprises three detected lensed images at the seeing-limited resolution. Such configuration is uncommon in galaxy-scale lensed systems, which typically present two or four lensed images (see, however,

Table 1. GTC/OSIRIS spectroscopic observations of the six BELLS GALLERY LAEs.

| LAE	PA (°)	Grism	Rest-frame spectral range (Å)	Resolution (km s^{-1})	Time (s)	Seeing (arcsec)	Depth (3σ) (10^{-17} erg s^{-1} cm^{-2} Å^{-1})
BG0201+3228	−47	R2000B; R2500R	1034–2010	230–200	2100; 2800	0.8	0.54–0.19
BG0742+3341	63	R2000B	1180–1695	230	3600	0.8	0.28
BG0755+3445	−30; 75	R2000B; R2500R	1086–2115	230–200	7200; 3600	0.8	0.10–0.16
BG0918+5104	10.8	R2000B; R2500R	1150–2260	230–200	7200; 3600	0.7	0.14–0.13
BG1429+1202	− 76.7	R2500V; R2500R	1150–2010	160–200	3600; 3600	0.8	0.19–0.17
BG1501+3042	29.8	R1000B	1000–2050	450	3000	1.1	0.20
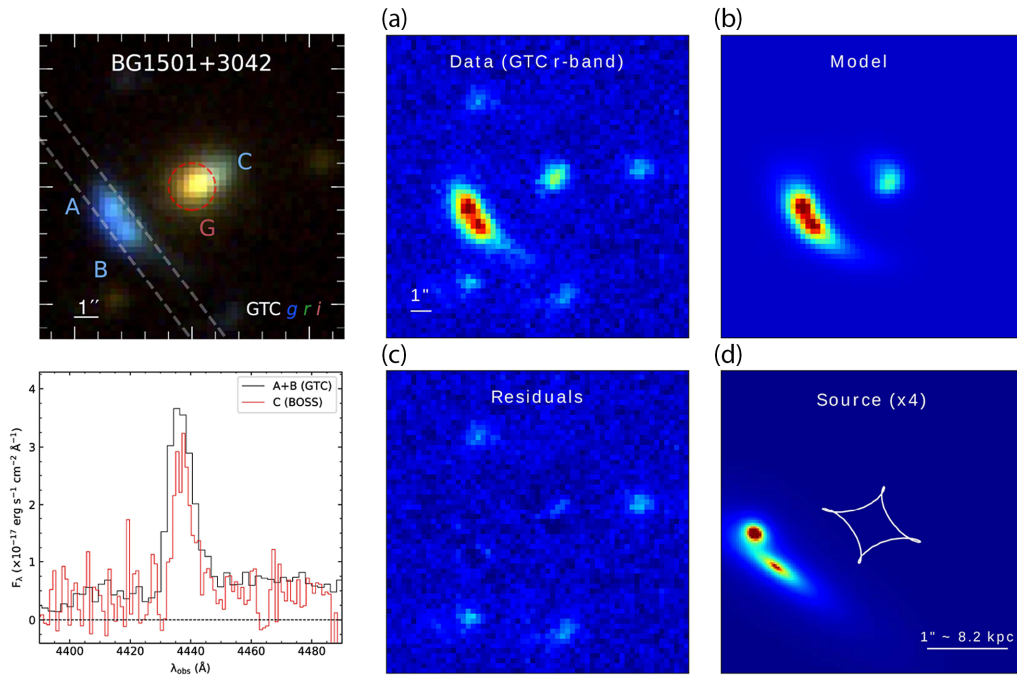
Figure 2. BG1501+3042, a new confirmed lensed LAE. Top left: GTC/OSIRIS rgb colour image (using *g* −, *r*-, and *i*-band images). The image is centred on the lensing galaxy (marked as 'G') and oriented such that north is up and east is to the left; bottom left: spectral region encompassing the Lyα line detected in the lensed images A+B (GTC/OSIRIS, black) and the counter-image C (SDSS/BOSS, red). Right-hand panels: GTC *r* band with the foreground lens subtracted (a), model with the predicted lensed images (b), final residuals from the best-fitting model (c), and position of the two components relative to the caustic (white) in the source plane (d). All panels are centred on the lensing galaxy.

other lensed configurations produced by groups or clusters of galaxies, e.g. Oguri et al. 2008; Dahle et al. 2013; Shu et al. 2018).

To understand this system in more detail, we use the 420 s GTC *r*-band image (≃0.9 arcsec FWHM) to perform the lens modelling for BG1501+3042. We use the same methodology already discussed in previous works (Bolton et al. 2008; Brownstein et al. 2012; Shu et al. 2015, 2016a,c; Marques-Chaves et al. 2017), consisting of a non-linear optimizer to minimize a χ^2 function using the Levenberg–Marquardt algorithm with the lmfit package (Newville et al. 2014). Briefly, the model assumes a mass distribution of the foreground lens parametrized as a singular isothermal ellipsoid, and an additional external shear is included to model the higher order effect from the environment.

The surface brightness distribution of both lens and background source is reconstructed parametrically using elliptical Sérsic models. The foreground-light model is combined with the predicted lensed images and convolved with the point spread function (PSF)

that was modelled with stars in the field of view of the GTC/OSIRIS image.

In a first attempt we modelled the system using a single source component. However, the model was not able to reproduce the three detected lensed images of BG1501+3042. To overcome this, we added a second source component to the model. In this case, our best-fitting model (χ^2/d.o.f. = 2428/3054) is able to recover reasonably well the light emission of the three observed lensed images. In this configuration, the lensed images 'A' and 'B' are the leading images of the two background sources, and image 'C' is composed of the blended emission from the two corresponding counter images. The lens model gives a total magnification $\mu = 3.2 \pm 0.5$. Table 2 summarizes the lensing magnification factors derived for the six LAEs studied in this work.

The projected separation between the centroids of the two components in the source plane is about 0.46 ± 0.06 arcsec which at $z = 2.645$ corresponds to 3.8 ± 0.6 kpc for the adopted cosmology, suggestive of a close interacting/merging system. Nevertheless,

Table 2. Properties of the six BELLS GALLERY LAEs.

	BG0201+3228	BG0742+3341	BG0755+3445	BG0918+5104	BG1429+1202	BG1501+3042	Notes
RA	02:01:21.39	07:42:49.68	07:55:23.52	09:18:59.21	14:29:54.80	15:01:14.61	(1)
Dec.	+32:28:29.7	+33:41:49.0	+34:45:39.6	+51:04:52.6	+12:02:35.6	+30:42:30.8	(1)
z_{lens}	0.3957 ± 0.0001	0.4936 ± 0.0001	0.7223 ± 0.0002	0.5811 ± 0.0002	0.5531 ± 0.0002	0.6384 ± 0.0002	(2)
z_{LAE}	2.8174 ± 0.0007	2.3625 ± 0.0009	2.6345 ± 0.0005	2.4000 ± 0.0003	2.8244 ± 0.0006	2.645 ± 0.001	(2)
g	20.94 ± 0.09	–	21.68 ± 0.10	21.69 ± 0.09	20.40 ± 0.04	21.32 ± 0.10	(3)
r	20.62 ± 0.08	–	21.16 ± 0.08	21.01 ± 0.09	20.14 ± 0.05	21.00 ± 0.05	(3)
i	20.47 ± 0.20^a	–	21.04 ± 0.06	20.91 ± 0.09	20.08 ± 0.05	20.98 ± 0.07	(3)
$F606W$	20.56 ± 0.05	22.18 ± 0.05	21.11 ± 0.05	20.87 ± 0.05	–	–	(3)
μ	15 ± 3	16 ± 3	14 ± 2	18 ± 3	8.8 ± 1.4	3.2 ± 0.5	(4)
β_{UV}	-1.50 ± 0.98	–	-1.59 ± 0.45	-1.58 ± 0.59	-1.76 ± 0.32	-1.96 ± 0.39	(5)
A_{UV}	1.71 ± 1.71	–	1.55 ± 0.82	1.56 ± 1.08	1.24 ± 0.58	0.87 ± 0.72	(5)
$E(B-V)$	0.20 ± 0.20	–	0.18 ± 0.10	0.19 ± 0.13	0.14 ± 0.07	0.10 ± 0.08	(5)
$F_{Ly\alpha}^{GTC}$	7.5 ± 0.3	7.1 ± 0.2	5.2 ± 0.2	3.0 ± 0.2	11.5 ± 0.2	4.1 ± 0.2	(6)
EW_0 (Lyα)	23 ± 6	45 ± 6	28 ± 5	16 ± 5	49 ± 7	16 ± 5	(6)
FWHM (Lyα)	395 ± 70	230 ± 50	330 ± 60	260 ± 60	290 ± 40	340 ± 150	(6)
Δv (Lyα)	230 ± 80	80 ± 70	80 ± 70	210 ± 80	30 ± 60	290 ± 120	(7)
Δv (ISM)	-100 ± 70	-20 ± 80	-150 ± 80	-10 ± 70	-230 ± 60	-175 ± 100	(7)
C_f (low-ISM)	0.67 ± 0.15	>0.51	0.66 ± 0.17	0.53 ± 0.11	0.44 ± 0.08	0.35 ± 0.17	(8)
C_f (H I)	0.96 ± 0.17	>0.93	0.95 ± 0.17	0.83 ± 0.14	0.68 ± 0.13	0.72 ± 0.13	(8)
M_{UV}	-22.06 ± 0.24	-19.95 ± 0.23	-21.43 ± 0.23	-21.05 ± 0.22	-23.04 ± 0.21	-23.12 ± 0.21	(9)
SFR (UV)	110_{-80}^{+470}	$\gtrsim 3$	55_{-30}^{+60}	40_{-25}^{+65}	175_{-70}^{+125}	135_{-55}^{+115}	(9)
$L_{Ly\alpha}$	4.43 ± 0.74	2.02 ± 0.32	2.48 ± 0.31	1.36 ± 0.19	30.67 ± 4.21	14.24 ± 1.93	(10)
SFR (Lyα)	$15.7_{-13.4}^{+103.3}$	$\gtrsim 1.0$	$7.3_{-4.5}^{+11.3}$	$4.1_{-2.9}^{+9.7}$	$63.2_{-30.7}^{+59.3}$	$17.4_{-9.7}^{+21.8}$	(10)
f_{esc} (Lyα)	0.14 ± 0.02	0.37 ± 0.02	0.14 ± 0.01	0.11 ± 0.01	0.36 ± 0.01	0.14 ± 0.01	(11)

Note. (1) Positions of the lens galaxy (J2000); (2) systemic redshifts of the lens (Shu et al. 2016b) and LAEs (Section 5.1); (3) integrated magnitudes of the LAEs in each band (AB); (4) lensing magnification factors derived in Shu et al. (2016c) for the first four lensed LAEs, Marques-Chaves et al. (2017) for BG1429+1202, and in Section 3 for BG1501+3042; (5) stellar UV continuum slope (equation 2), UV dust extinction (AB mag, equation 3), and colour excess of the stellar continuum assuming the Reddy et al. (2015) attenuation curve; (6) observed flux (units of 10^{-16} erg s^{-1} cm^{-2}), rest-frame equivalent width (Å), and full width at half-maximum (km s^{-1}) of the Lyα line; (7) centroid velocity of Lyα and ISM absorption lines (average) relative to the systemic redshift (km s^{-1}); (8) low-ISM and H I covering fractions using the depth of the average absorption line profile of ISM lines (Si II 1260 Å, C II 1334 Å, and Si II 1526 Å) and using the relation of Gazagnes et al. (2018), respectively; (9) intrinsic UV absolute magnitudes (AB) and star formation rates (M$_\odot$ yr^{-1}; equation 4); (10) intrinsic Lyα luminosity (units of 10^{42} erg s^{-1}) and star formation rates (M$_\odot$ yr^{-1}; equation 9); and (11) Lyα escape fraction.
^{a}The ACAM/WHT *i*-band data of BG0201+3228 are affected by a high background level.

we cannot confirm unambiguously the merging scenario as no velocity offset between the lensed images 'A' and 'B' is clearly detected in the available spectrum (with a resolution of $\simeq 450$ km s^{-1} FWHM). The sources have effective radius $R_{eff}^A = 1.17 \pm 0.47$ kpc and $R_{eff}^B = 3.30 \pm 0.31$ kpc.

4 RESULTS FROM IMAGING DATA

4.1 Photometry

As seen in Fig. 1 the morphology of the LAEs in this sample consists of complex arc-like features with multiple lensed images seen in the observer plane.

Given the typical ~ 0.8 arcsec FWHM seeing of the GTC, WHT, and CFHT images, there is light contamination from the foreground lens galaxies. In order to perform a clean photometry of the lensed images, we use the two-dimensional fitting program GALFIT (Peng et al. 2002, 2010) to model and substract the light distribution of the foreground lens (and in some cases additionally nearby objects). We use Sérsic profiles centred at the centroids of each LRG light emission allowing only two pixels freedom (~ 0.5 arcsec). For the four lensed LAEs with *HST* imaging, we use the models of the foreground lens presented in Shu et al. (2016c) as priors in our modelling (i.e. effective radius, minor-to-major axial ratio, and major-axis position angle). Nearby stars were used as PSF models.

We further use SEXTRACTOR (Bertin & Arnouts 1996) to measure the magnitudes in each band. To do so, we use aperture photometry using apertures with diameters of 2.5 times the FWHM of the PSF. Aperture photometry was performed for compact lensed morphologies, such as the lensed images of BG0755+3445, BG1429+1202 and the faint lensed counter-images of BG0201+3228 or BG1501+3042. For more complex morphologies, such as bright extended arcs seen in BG0201+3228, BG0918+5104 and BG1501+3042, we derived total magnitudes using the corresponding SEXTRACTOR's MAG AUTO output. Table 2 summarizes the photometric measurements for each lensed LAE.

4.2 UV luminosity

Knowing the total magnification of these galaxies, we determine the intrinsic absolute UV magnitude (M_{UV} in units of AB magnitudes) in the rest-frame UV, typically defined at ≈ 1500–1700 Å:

$$M_{UV} = m - 5 \log_{10}(D_L) + 5 + 2.5 \log_{10}(1 + z) + 2.5 \log_{10}(\mu),$$
(1)

where m is the apparent AB magnitude in the closest observed band to the rest-frame 1600 Å (corrected for the Galactic dust extinction using the values from Schlafly & Finkbeiner 2011), D_L is the luminosity distance in pc at a given redshift (z), and μ is the total magnification factor.

We use the *HST F606W* band ($\lambda_{\mathrm{eff}} = 5778$ Å) to trace the rest-frame 1600 Å of BG0742+3341 ($z = 2.363$) and BG0918+5104 ($z = 2.400$), whereas for the highest redshift LAEs we use the ground-based *r*-band apparent magnitudes ($\lambda_{\mathrm{eff}} = 6231$ Å). These LAEs span a wide range of M_{UV}, from -19.9 to -23.1 AB (see Table 2).

4.3 Beta slope, dust attenuation, and star formation rate

The stellar UV continuum slope β_{UV} is a useful indicator of the dust content in star-forming galaxies, in the sense that larger quantities of dust produce redder UV SEDs. Assuming a simple power law $f_\lambda \propto \lambda^{\beta_{\mathrm{UV}}}$, the slope can be estimated as

$$\beta_{\mathrm{UV}} = -\frac{m_1 - m_2}{2.5 \log_{10}(\lambda_{m_1}/\lambda_{m_2})} - 2. \tag{2}$$

We use the r ($m_1, \lambda_1 = 6231$ Å) and i ($m_2, \lambda_2 = 7625$ Å) bands, which at $z = 2.4$–2.8 correspond to a rest-frame spectral coverage of about 1600–2200 Å. Following Reddy et al. (2015), β_{UV} is correlated with the dust extinction at $\lambda = 1600$ Å, A_{UV}, in the form

$$A_{\mathrm{UV}} = 1.84(\beta_{\mathrm{UV}} - \beta_{\mathrm{UV},0}) = k_{\mathrm{UV}} \times E(B - V), \tag{3}$$

where $\beta_{\mathrm{UV},0} = -2.44$ and represents the intrinsic UV spectral slope in the absence of dust, k_{UV} is the attenuation coefficient at 1600 Å ($\simeq 8.34$; Reddy et al. 2015), and $E(B - V)$ is the colour excess of the stellar continuum. Although not relevant here (see Section 5.4), we consider similar $E(B - V)$ for stellar and nebular components (e.g. Koyama et al. 2015; Faisst et al. 2019).

Finally, using the Kennicutt's conversion (Kennicutt 1998), the rest-frame UV luminosity (already corrected for the lensing magnification) can be translated into an intrinsic UV star formation rate (in units of $M_\odot$ yr^{-1}):

$$\mathrm{SFR(UV)} = 1.48 \times 10^{-28} \times L_{\mathrm{UV}} \times 10^{0.4 A_{\mathrm{UV}}}. \tag{4}$$

Note that, however, this expression assumes the standard Salpeter (1955) stellar initial mass function (IMF). In order to correct for the lower proportion of low-mass stars (e.g. Chabrier 2003, IMF), we divide the SFR by 1.8.

Measurements of β_{UV}, A_{UV}, $E(B - V)$, and lensing- and dust-corrected SFRs (UV) for all LAEs are listed in Table 2. For comparison, adopting the Calzetti et al. (2000) extinction law we would find values of A_{UV} slightly larger (3–15 per cent, depending on each LAE) than the ones measured using equation (3), yielding also to larger SFRs (3–25 per cent). On the other hand, some authors argue that young and low-mass galaxies are better modelled with an extinction curve close to the Small Magellanic Cloud (SMC; e.g. Bouwens et al. 2016; Reddy et al. 2018; Álvarez-Márquez et al. 2019). Adopting the SMC extinction curve, we would find SFRs lower by a factor of ≈ 2.

5 REST-FRAME UV SPECTRA

In this Section we analyse the rest-frame UV spectra of these lensed LAE systems. All spectra, shown in Fig. 3, have relatively high S/N per pixel in the continuum, despite the short exposure time, ranging from ~ 7 for the faintest LAE (BG0742+3341) to ~ 20 for the brightest ones. These spectra show prominent Lyα emission spatially coincident with the lensed images of the background LAEs. The achieved S/N is also sufficient to detect a wealth of other absorption/emission features associated with the photospheres and winds of massive stars, neutral and slightly ionized interstellar

medium gas (ISM), and ionized gas in H II regions. The spectrum of BG0742+3341 exhibits a redder UV slope than in the other LAEs, suggesting a significant foreground light contamination from the lens galaxy (this LRG is bright and is relatively close to the arc, $\lesssim 1$ arcsec). For the remaining LAEs, in particular for BG1429+1202 and BG1501+3042, we do not expect a large light contamination in their spectra (< 10 per cent), since the bright lensed images covered by the GTC long slits are far away from the lens galaxies ($\simeq 1.7$–3 arcsec).

5.1 Galaxy systemic redshifts

Systemic redshifts are measured using stellar absorption lines, generated in the photospheres of stars, and nebular emission from H II regions. In the absence of a clear detection of nebular or stellar features we also use the Si II* fine-structure emission lines in deriving the systemic redshift. These lines (Si II* 1197 Å, Si II* 1264 Å, and Si II* 1533 Å) are produced by resonant scattering and re-emission of ground-state interstellar absorption features, and as already shown in France et al. (2010), Steidel et al. (2016) and Jones, Stark & Ellis (2018), they are useful for the determination of the galaxy rest velocity when observed with significant high spectral resolution, avoiding the contamination from the neighbouring red component of resonance absorption features (Si II 1193 Å, Si II 1260 Å, and Si II 1526 Å, respectively). This is demonstrated in the top panels of Fig. 4, where we compare the spectral profiles of Si II* 1264 Å in two LAEs (BG0755+3445 and BG1429+1202, left and right, respectively) to those of nebular emission ([C III] 1906 Å) and stellar photospheric absorption (C III 1247 Å) on the systemic velocity of each galaxy. Si II* emission lines agree with the nebular and stellar redshifts within a rms of $\lesssim 50$ km s^{-1}.

We now list the most prominent lines used for the measurements of the systemic redshifts of each LAE.

BG0201+3228 shows several faint stellar photospheric absorption lines including C III 1247 Å, Si III 1294,1298 Å, and C III 1426 Å. We use the mean of them to derive the rest-velocity of BG0201+3228 as $z_{\mathrm{sys}} = 2.8174 \pm 0.0007$. Nebular O III] 1666 Å and C III] 1906,1908 Å emission lines are only barely detected ($\sim 2\sigma$; they fall in regions of relatively strong night sky lines), making their measurements difficult.

For BG0742+3341, due to the limited wavelength range of its spectrum, from 1180 to 1700 Å in the rest frame (it was not observed with the R2500R grism), and the relatively modest S/N continuum spectrum (BG0742+3341 is the faintest LAE in our sample), we do not detect clearly any photospheric stellar absorption line or nebular emission. Nevertheless, we clearly detect three fine-structure emission lines, Si II* 1197 Å, Si II* 1264 Å, and Si II* 1533 Å, at a redshift $z = 2.3625 \pm 0.0009$. We thus assume the redshift of the fine-structure emission lines as the systemic redshift of BG0742+3341.

The combined spectrum of BG0755+3445 (covering the four lensed images, A to D in Fig. 1) shows a prominent and resolved C III] 1906, 1908 Å nebular emission at $z_{\mathrm{neb}} = 2.6345 \pm 0.0005$ (see Fig. 4), as well as faint stellar photospheric absorption lines, such as C III 1247 Å and Si III 1298 Å, at $z_{\mathrm{stars}} = 2.6340 \pm 0.0007$. We use both nebular emission and stellar absorption lines to measure the systemic redshift $z_{\mathrm{sys}} = 2.6342 \pm 0.0008$.

For BG0918+5104, several nebular emission lines are detected with high significance ($\sigma \gtrsim 5$), including the O III] 1660, 1666 Å and Si III] 1882, 1892 Å doublets, for which we derive the systemic redshift of $z_{\mathrm{sys}} = 2.4000 \pm 0.0003$ (see Fig. 4). The
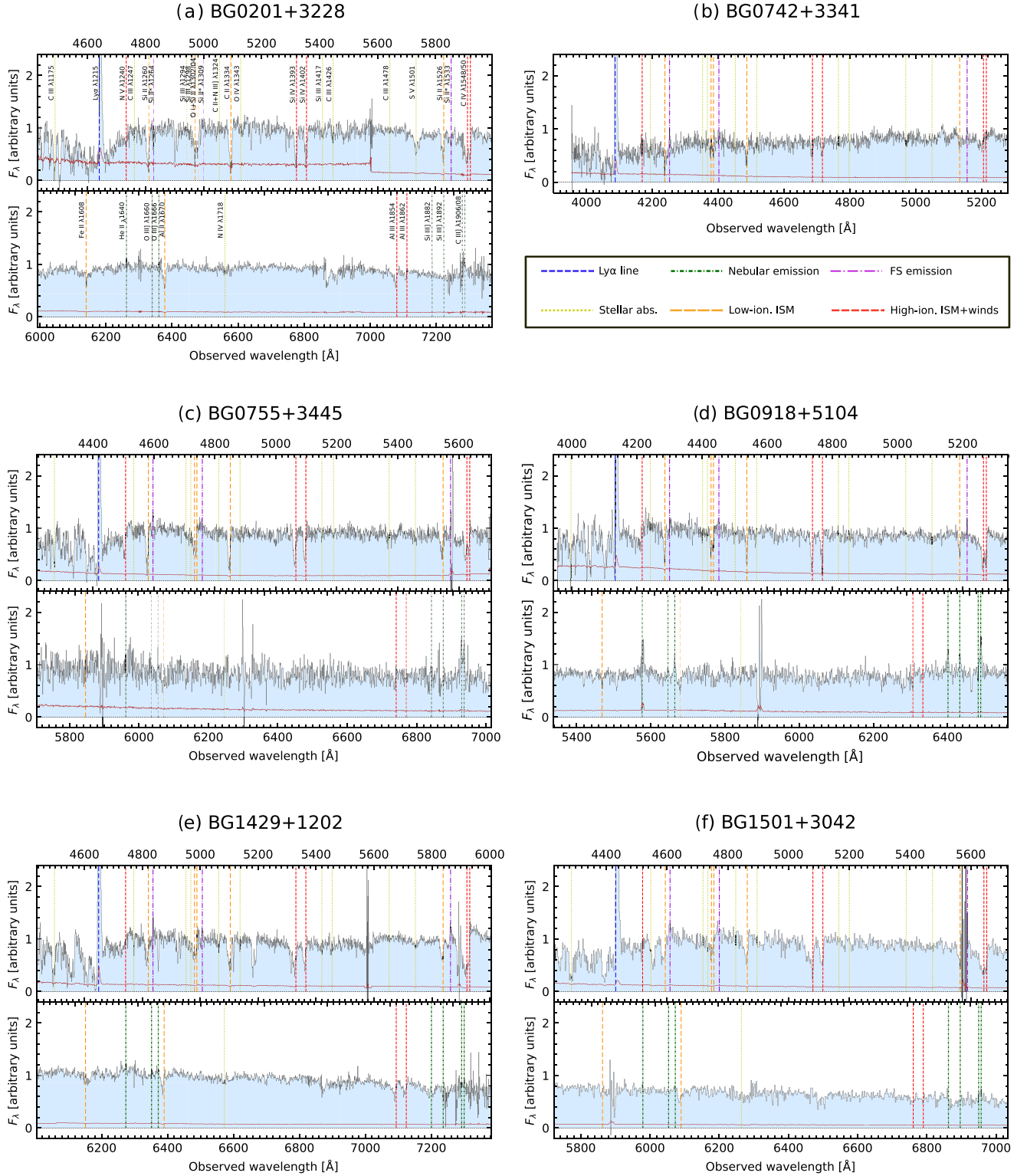
Figure 3. Portions of the rest-frame UV spectra of the six LAEs observed with OSIRIS. From panels (a) to (f) we show, respectively, the spectra of BG0201+3228, BG0742+3341, BG0755+3445, BG0918+5104, BG1429+1202, and BG1501+3042. Ticks mark the position of the Lyα line (blue) as well as other main features associated with nebular emission (green), fine-structure emission (purple), stellar photospheric absorption (yellow), low-ionization ISM absorption (orange), and high-ionization ISM absorption and stellar winds (P-Cygni profiles, red). The 1σ uncertainty (per spectral element) is plotted in red.
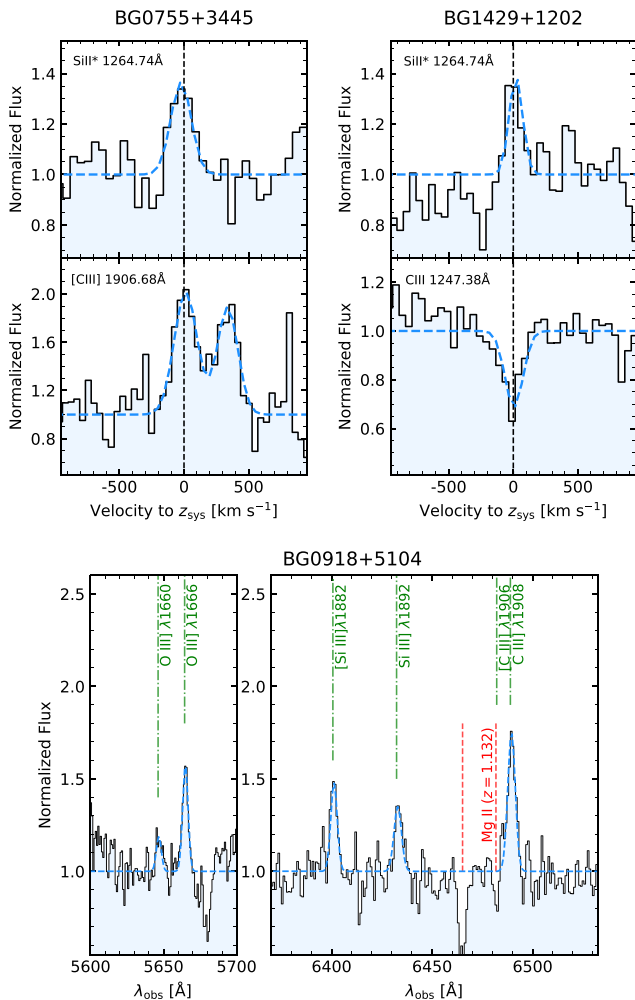
Figure 4. Determination of the systemic redshifts. *Top*: Comparison between the spectral profiles on rest velocity of fine-structure Si II* 1264 Å emission lines (top panels) in BG0755+3445 and BG1429+1202 (left and right, respectively) and those of H II emission ([C III] 1906 Å , bottom left) and stellar absorption (C III 1247 Å, bottom right). Fine-structure emission lines agree with the nebular and stellar redshifts within a rms of $\lesssim 50\,\mathrm{km\,s^{-1}}$. *Bottom:* Nebular emission lines in BG0918+5104 for which the systemic redshift of $z = 2.4000 \pm 0.0003$ was measured. [C III] 1906 Å nebular emission is highly affected by the absorption of the Mg II $\lambda 2796, 2803$ doublet from an intervening absorption system at $z = 1.312 \pm 0.001$ (see Section A).

nebular C III] 1908 Å emission is also detected with high significance, but not the corresponding [C III] 1906 Å line, whose profile is highly affected by the absorption of the Mg II 2796, 2803 Å doublet from an intervening absorption system at $z = 1.312 \pm 0.001$ (see Appendix A for more details). In addition, the fine-structure emission line Si II* 1533 Å is also detected at $z_{\mathrm{FS}} = 2.4004 \pm 0.0006$, consistent with the systemic redshift from H II regions.

The new spectroscopic observations of BG1429+2102 allow us to identify several photospheric absorption features, C III 1247 Å, Si III 1294, 1298 Å, the close blend of C II and N III 1324 Å, S V 1501 Å, and N IV 1718 Å, and redefine the systemic redshift of BG1429+1202 as $z_{\mathrm{sys}} = 2.8244 \pm 0.0006$, similar to the one measured by Rigby et al. (2018a) ($z_{\mathrm{sys}} = 2.8241 \pm 0.0006$). Emission in nebular lines of O III] 1666 Å and C III] 1906, 1908 Å

is also detected, but with low significance. Fine-structure emission lines Si II* 1264 Å, Si II* 1309 Å, and Si II* 1533 Å are also clearly detected and their peak lie at $z_{\mathrm{FS}} = 2.8243 \pm 0.0008$, consistent with the systemic redshift derived using photospheric absorption lines (see top right panel of Fig. 4).

Finally, despite the relatively modest S/N continuum and the low spectral resolution provided by the R1000B grism ($\sim 450\,\mathrm{km\,s^{-1}}$), the spectrum of BG1501+3042 shows both stellar absorption lines (Si III 1294 Å, C II and Si III 1296 Å, and Si III 1298 Å), and nebular emission lines in O III] 1666 Å and C III] 1906, 1908 Å for which we measure the systemic redshift $z_{\mathrm{sys}} = 2.645 \pm 0.001$.

5.2 ISM absorption lines

The strongest absorption features seen in the spectra of these LAEs in Fig. 3 are associated with the ISM gas and are produced by the resonance transition of several ionic species (e.g. H, C, O, Al, Si, Fe, among others). We detect several ISM absorption lines in a variety of ionization stages, from neutral or partially neutral (e.g. O I, Si II, C II), to highly ionized species (e.g. Al III, Si IV, or C IV), which predominantly trace gas at higher temperatures.

Since ISM absorption lines are seen against the continuum provided by the integrated light of O and B stars in a galaxy, they offer a unique probe of the kinematics of the gas. It is well accepted that large-scale galactic outflows are ubiquitous in nearly all star-forming galaxies due the kinetic energy deposited by stellar and supernova-driven winds. Such signatures have been evaluated from blueshifted ISM absorption lines with respect to the systemic redshift (e.g. Shapley et al. 2003; Weiner et al. 2009; Steidel et al. 2010), i.e. the gas on the near side of the galaxy is moving towards the observer.

We fit symmetric Gaussian profiles to the low- and high-ionization ISM lines that are detected with high significance ($>5\sigma$). The strength (i.e. rest-frame equivalent widths, EW_0), the intrinsic FWHM (corrected for the instrumental broadening, see Table 1), and the residual intensity (I/I_0) of the ISM lines are listed in Table 3. Note however that the measurements of EW_0 and I/I_0 in BG0742+3341 should be regarded as lower and upper limits, respectively, due to the foreground light contamination of the lens galaxy in its spectrum. Nevertheless, this effect does not change the main results of this work. Almost all lines appear spectrally resolved, even for BG1501+3042, whose spectrum was recorded with low spectral resolution. The exception is BG0742+3341, in which the low-ionization ISM lines appear spectrally unresolved (with intrinsic FWHM $< 230\,\mathrm{km\,s^{-1}}$).

Most LAEs show ISM absorption lines blueshifted to their systemic redshifts. The velocity offset is noticeable for the most luminous LAEs, BG0201+3228, BG0755+3445, BG1429+1202, and BG1501+3042, where the ISM absorption lines appear blueshifted by -100 ± 70, -150 ± 80, -230 ± 60, and $-175 \pm 100\,\mathrm{km\,s^{-1}}$, respectively. On the other hand, for the less luminous LAEs, BG0742+3341 and BG0918+5104, the ISM absorption lines have the minimum intensity close to (and consistent with) the systemic velocities. Nevertheless, for these ones the spectral profiles appear slightly asymmetric with a pronounced blueshifted absorption tail. Fig. 5 (lower panels) shows the velocity plots of several normalized low-ionization ISM absorption lines, relative to the systemic redshift of each lensed LAE measured in Section 5.1.

The strength of the ISM lines also depends on the geometric covering fraction of the gas, C_{f}, and the ion column density, N. The

Table 3. ISM absorption line features.

LAE[1]	Ion[2]	$\lambda_{rest}^{(3)}$ (Å)	$\Delta v^{(4)}$ (km s^{-1})	FWHM[5] (km s^{-1})	$EW_0^{(6)}$ (Å)	$I/I_0^{(7)}$
BG0201+3228	Si II	1260.42	-155 ± 60	480 ± 65	2.52 ± 0.31	0.17 ± 0.09
	O I	1302.16	-21 ± 80	510 ± 80	2.31 ± 0.30	0.27 ± 0.08
	Si II	1304.37	-85 ± 80	440 ± 80	1.64 ± 0.26	0.48 ± 0.06
	C II	1334.53	-20 ± 60	540 ± 65	3.07 ± 0.32	0.13 ± 0.10
	Si IV	1393.76	-90 ± 60	350 ± 70	1.65 ± 0.23	0.23 ± 0.09
	Si IV	1402.77	-70 ± 60	375 ± 70	1.52 ± 0.24	0.24 ± 0.09
	Si II	1526.70	-126 ± 60	415 ± 75	1.61 ± 0.21	0.34 ± 0.07
	C IV	1548.20	-240 ± 9	560 ± 90	2.27 ± 0.28	0.35 ± 0.07
	C IV	1550.78	-80 ± 90	280 ± 90	1.21 ± 0.18	0.47 ± 0.07
	Fe II	1608.45	-300 ± 90	<200	0.50 ± 0.08	0.65 ± 0.05
	Al II	1670.78	-40 ± 60	285 ± 80	1.11 ± 0.15	0.57 ± 0.05
	Al III	1854.72	-130 ± 75	285 ± 80	0.62 ± 0.12	0.58 ± 0.05
	Al III	1862.80	-120 ± 75	<200	0.27 ± 0.05	0.76 ± 0.05
BG0742+3341	Si II	1260.42	-35 ± 80	<230	0.62 ± 0.14	0.21 ± 0.19
	O I	1302.16	-100 ± 90	<230	0.41 ± 0.10	0.66 ± 0.18
	Si II	1304.37	-85 ± 90	<230	0.30 ± 0.08	0.71 ± 0.18
	C II	1334.53	15 ± 70	<230	0.60 ± 0.13	0.42 ± 0.15
	Si IV	1393.76	-160 ± 70	190 ± 70	0.58 ± 0.13	0.64 ± 0.13
	Si IV	1402.77	-50 ± 70	280 ± 80	0.62 ± 0.15	0.68 ± 0.13
	Si II	1526.70	-70 ± 80	<230	0.17 ± 0.06	0.77 ± 0.21
	C IV	1548.20	-320 ± 100	300 ± 100	0.58 ± 0.16	0.71 ± 0.18
	C IV	1550.78	-200 ± 100	<230	0.14 ± 0.05	0.67 ± 0.18
BG0755+3445	Si II	1260.42	-180 ± 70	415 ± 80	1.62 ± 0.19	0.18 ± 0.09
	O I	1302.16	-65 ± 60	365 ± 70	0.91 ± 0.09	0.55 ± 0.05
	Si II	1304.37	-140 ± 65	<230	0.65 ± 0.07	0.49 ± 0.06
	C II	1334.53	-200 ± 60	430 ± 70	1.78 ± 0.19	0.24 ± 0.08
	Si IV	1393.76	-220 ± 65	480 ± 80	1.56 ± 0.16	0.33 ± 0.07
	Si IV	1402.77	-225 ± 65	360 ± 70	1.16 ± 0.13	0.41 ± 0.07
	Si II	1526.70	-120 ± 65	480 ± 70	1.25 ± 0.14	0.48 ± 0.06
	C IV	1548.20	-320 ± 90	465 ± 90	1.45 ± 0.16	0.45 ± 0.06
	C IV	1550.78	-290 ± 90	280 ± 90	0.62 ± 0.07	0.55 ± 0.05
BG0918+5104	Si II	1260.42	-15 ± 60	385 ± 80	1.27 ± 0.21	0.38 ± 0.11
	O I	1302.16	-10 ± 65	200 ± 85	0.70 ± 0.12	0.49 ± 0.10
	Si II	1304.37	-80 ± 65	290 ± 80	0.62 ± 0.10	0.63 ± 0.06
	C II	1334.53	-3 ± 60	240 ± 60	1.09 ± 0.18	0.33 ± 0.12
	Si IV	1393.76	-120 ± 60	350 ± 70	1.44 ± 0.25	0.26 ± 0.12
	Si IV	1402.77	-85 ± 65	320 ± 70	1.29 ± 0.22	0.23 ± 0.13
	Si II	1526.70	15 ± 65	250 ± 70	0.75 ± 0.13	0.55 ± 0.07
	C IV	1548.20	-170 ± 100	550 ± 150	2.04 ± 0.4	0.28 ± 0.12
	C IV	1550.78	-160 ± 80	<200	0.74 ± 0.15	0.37 ± 0.11
	Al II	1670.78	-6 ± 60	<200	0.73 ± 0.15	0.68 ± 0.11
BG1429+1202	Si II	1260.42	-250 ± 55	550 ± 55	1.28 ± 0.10	0.59 ± 0.07
	O I	1302.16	-160 ± 60	435 ± 60	0.81 ± 0.09	63 ± 0.04
	Si II	1304.37	-160 ± 60	255 ± 60	0.54 ± 0.06	0.61 ± 0.04
	C II	1334.53	-170 ± 55^a	710 ± 80^a	1.47 ± 0.13^a	0.40 ± 0.05^a
	Si IV	1393.76	-250 ± 50^a	750 ± 80^a	2.01 ± 0.21^a	0.34 ± 0.07^a
	Si IV	1402.77	-240 ± 50	495 ± 50	1.13 ± 0.10	0.38 ± 0.06
	Si II	1526.70	-205 ± 50	460 ± 60	1.07 ± 0.09	0.61 ± 0.05
	C IV	1548.20	-590 ± 90^b	1100 ± 150^b	4.28 ± 0.41^b	0.25 ± 0.07^b
	C IV	1550.78	-590 ± 90^b	1100 ± 150^b	4.28 ± 0.41^b	0.25 ± 0.07^b
	Al II	1670.78	-195 ± 50	320 ± 50	0.68 ± 0.07	0.71 ± 0.05
	Al III	1854.72	-200 ± 75	385 ± 70	0.81 ± 0.09	0.61 ± 0.05
	Al III	1862.80	-230 ± 70	450 ± 70	0.78 ± 0.09	0.75 ± 0.04
BG1501+3042	Si II	1260.42	-310 ± 100^a	850 ± 150^a	1.97 ± 0.35^a	0.56 ± 0.10^a
	O I	1302.16	-250 ± 100^c	725 ± 125^c	1.27 ± 0.25^c	0.64 ± 0.08^c
	Si II	1304.37	-250 ± 100^c	725 ± 125^c	1.27 ± 0.25^c	0.64 ± 0.08^c
	C II	1334.53	-190 ± 90	550 ± 100	1.73 ± 0.40	0.48 ± 0.11
	Si IV	1393.76	-180 ± 100^a	770 ± 150^a	2.81 ± 0.45^a	0.23 ± 0.12^a
	Si IV	1402.77	-210 ± 90	480 ± 100	1.85 ± 0.35	0.51 ± 0.09
	Si II	1526.70	-140 ± 90	<500	1.16 ± 0.21	0.67 ± 0.15

Table 3 – *continued*

LAE[(1)]	Ion[(2)]	$\lambda_{\mathrm{rest}}^{(3)}$ (Å)	$\Delta v^{(4)}$ (km s^{-1})	FWHM[(5)] (km s^{-1})	$EW_0^{(6)}$ (Å)	$I/I_0^{(7)}$
	C IV	1548.20	-420 ± 200^b	1100 ± 250^b	4.5 ± 0.50^b	0.40 ± 0.13^b
	C IV	1550.78	-420 ± 200^b	1100 ± 250^b	4.5 ± 0.50^b	0.40 ± 0.13^b
	Al II	1670.78	-190 ± 100	<500	0.73 ± 0.25	0.72 ± 0.07

Note. (1) LAE; (2) ion; (3) vacuum wavelength in the rest frame; (4) centroid velocity relative to the systemic redshift; (5) full width at half-maximum corrected for the instrumental broadening; (6) rest-frame equivalent width; and (7) ratio between the residual intensity of the line and the continuum level.

^{a}Affected by other absorption lines from intervening systems at lower redshifts.

^{b}Refers to the C IV 1548,1550 Å doublet.

^{c}Refers to the blended O I 1302 Å and Si II 1304 Å absorption

covering fraction of an ion can be estimated from

$$C_\mathrm{f} = \frac{1 - I/I_0}{1 - e^{-\tau}}, \qquad (5)$$

where I is the residual intensity, I_0 the continuum level, and τ is the optical depth of an absorption line, that is related with N (in units of cm^{-2}) by (Savage & Sembach 1991)

$$\tau = Nf\lambda \frac{\pi e^2}{m_e c} = \frac{Nf_{\mathrm{osc}}\lambda}{3.768 \times 10^{14}}, \qquad (6)$$

where f_{osc} and λ are the ion oscillator strength (Morton 1991) and the transition wavelength (Å). However, ISM lines in LBGs and LAEs present typically saturated profiles when observed with high spectral resolution (e.g. Pettini et al. 2002; Dessauges-Zavadsky et al. 2010; Jones, Stark & Ellis 2012; Jones et al. 2013; Marques-Chaves et al. 2018). To test if some of these lines are saturated or not, we consider the linear part of the curve of growth and use the ratios of EW_0 of different transitions of a given ion. In such case, considering the three transitions of Si II detected in our spectra, at 1260, 1304, and 1526 Å, we would expect ratios of $EW_0(1260\,\text{Å})/EW_0(1526\,\text{Å}) \simeq 5$, $EW_0(1260\,\text{Å})/EW_0(1304\,\text{Å}) \simeq 10$, and $EW_0(1304\,\text{Å})/EW_0(1526\,\text{Å}) \simeq 0.5$. However, our LAEs show average values of $EW_0(1260\,\text{Å})/EW_0(1526\,\text{Å}) = 1.8 \pm 0.9$, $EW_0(1260\,\text{Å})/EW_0(1304\,\text{Å}) = 2.1 \pm 0.3$, and $EW_0(1304\,\text{Å})/EW_0(1526\,\text{Å}) = 0.9 \pm 0.4$, suggesting that these transitions are likely saturated.

We thus assume the optically thick regime, i.e. $\tau \gg 1$, so that equation (5) simplifies to $C_\mathrm{f} = 1 - I/I_0$. In order to minimize the statistical uncertainty we derive the average absorption line profile of ISM lines using the low-ionization metal lines Si II 1260 Å, C II 1334 Å, and Si II 1526 Å. Fig. 5 shows the normalized intensity as a function of velocity of these ISM lines. The estimated covering fractions using the three low-ionization metal-absorption lines, C_f (low-ISM), are between $\sim$0.3–0.7. For BG0742+3341, the measured C_f (low-ISM) should be regarded as a lower limit as all low-ISM lines appear spectrally unresolved. The same may apply for BG1501+3042 whose spectrum was recorded with low spectral resolution ($\simeq 450$ km s^{-1} FWHM). Although ISM lines are spectrally resolved for this LAE, the measured values of I/I_0 are likely overestimated.

Reddy et al. (2016b) found that low-ionization metal-absorption lines have covering fractions smaller than those from the H I gas. From the analysis of H I and low-ionization ISM lines of 18 star-forming galaxies, Gazagnes et al. (2018) found that the Si II 1260 Å covering fraction scales linearly with the H I covering fraction (equation (12) in Gazagnes et al. 2018; see also Chisholm et al. 2018). Assuming again that the gas is optically thick, we use the values of I/I_0 of the low-ionization Si II 1260 Å line (see Table 3)

to measure the C_f (Si II). Following Gazagnes et al. (2018), we find C_f (H I) between $\simeq$ 0.68–0.96, larger than those measured using the average absorption line profile of ISM lines. All measurements are listed in Table 2. In Section 6, we discuss our measurements with those obtained for other LAEs and LBGs (Jones et al. 2013; Shibuya et al. 2014b).

5.3 Stellar metallicity from stellar population synthesis models

The most massive and hottest stars also produce strong outflows of material. The resulting spectral profile is characterized by a redshifted emission with a corresponding blueshifted absorption produced by material moving away from the stars (also called P-Cygni profile). The strength of P-Cygni profiles depends on the density of stellar winds and therefore, on the mass-loss rate, which is dependent on the stellar metallicity. Because wind lines are produced by the most massive stars, P-Cygni profiles are also sensitive to the age and IMF of the stellar population. The most prominent stellar wind features in the UV are the N V 1238,1242 Å and C IV 1548,1550 Å high-ionization lines.

In order to study the stellar wind features in our LAEs, we generate high-resolution (0.4 Å) continuum-normalized UV spectra computed with the spectral synthesis code STARBURST99[3] (Leitherer et al. 1999, 2010). Standard Geneva tracks with stellar metallicities ($Z_*/Z_\odot$, assuming $Z_\odot = 0.02$) of 0.05, 0.2, 0.4, 1.0, and 2.0 were generated. We consider models with continuous star formation histories with a fixed age of 100 Myr and an IMF with a power slope index $\alpha = -2.35$ over the mass range $0.5 < M_*/\mathrm{M}_\odot < 100$ to minimize the well-known metallicity–age–IMF degeneracy. We are aware on the limitations of these models, particularly in fixing the age of 100 Myr. Note, however, that continuous star formation models reach equilibrium in the UV in a few tens of Myr, after which become almost time independent (e.g. Cabanac, Valls-Gabaud & Lidman 2008; James et al. 2014; Steidel et al. 2016; Marques-Chaves et al. 2018). Therefore, our models are still valid for ages $\gtrsim$30 Myr. Considering different star formation histories (burst), and the age or IMF as free parameters would introduce large systematics in our analysis given the limited S/N of our spectra.

The analysis is performed in the wind N V and C IV lines, those that show prominent P-Cygni profiles. Our GTC spectra do not show any clear wind features in other lines that are conspicuous in the spectra of individual O stars (O V 1371 Å, Si IV 1383,1402 Å, or N IV 1719 Å), suggesting that the more numerous B stars are diluting the contribution of the O stars. STARBURST99 outputs were
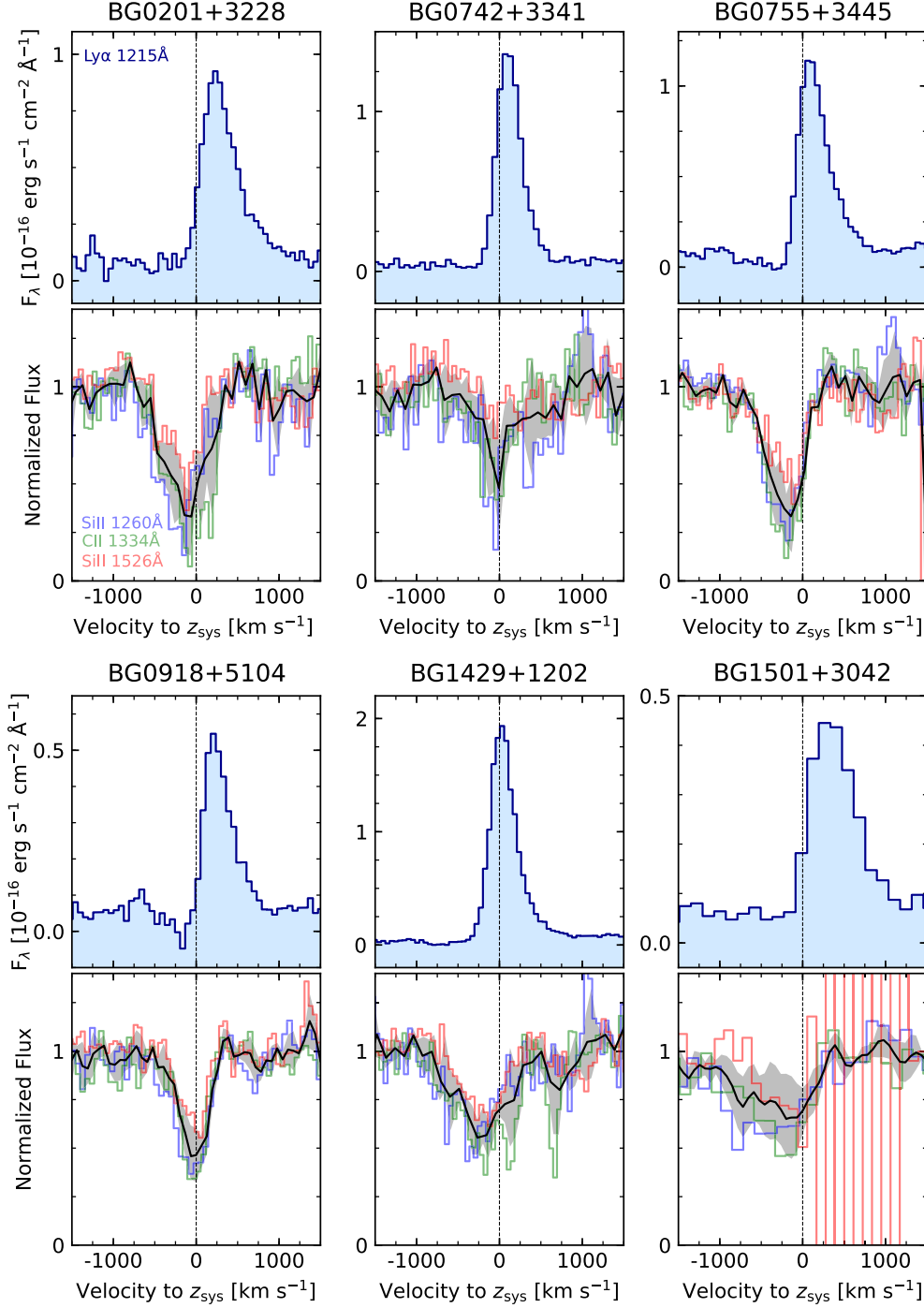
---

[3]http://www.stsci.edu/science/starburst99/docs/default.htm

Figure 5. Lyα emission (upper panels) and low-ionization interstellar absorption features (lower panels; Si II 1260 Å, C II 1334 Å, and Si II 1526 Å in blue, green, and red, respectively) on the systemic velocity (measured using stellar absorption, nebular and fine-structure emission lines, see Section 5.1). Lyα appears to be redshifted, while the interstellar absorption lines are blueshifted (average profile in black with the standard deviation in grey shadow), which is consistent with galaxy-scale outflows of material from these galaxies in the form of a wind, similar to those seen in other star-forming galaxies at $z \sim 3$ (e.g. Shapley et al. 2003; Steidel et al. 2010). The interstellar absorption lines in the LAEs BG0742+3341 and BG0918+5104 show, however, a minimum intensity close to the systemic velocity of these galaxies.

smoothed to the spectral resolution of our GTC spectra and rebined to a spectral element of 0.58 Å pix^{-1}. The GTC spectra were firstly normalized using local continuum windows that are free of strong absorption and emission features. Large spectral windows were used in the fit (marked in grey in Fig. 6) to account for stellar winds with terminal velocities exceeding $\sim$2000 km s^{-1} (e.g. Pettini et al. 2000;

Marques-Chaves et al. 2018), from 1233–1250 Å for N V and 1537–1559 Å for C IV. We exclude in the fit spectral regions affected by strong sky-subtracted residuals and strong interstellar absorption (in C IV, from 1539–1552 Å) as well as other absorption lines produced by intervening systems at lower redshifts (see Appendix A). We exclude BG0742+3341 in this analysis, due to the low S/N in the
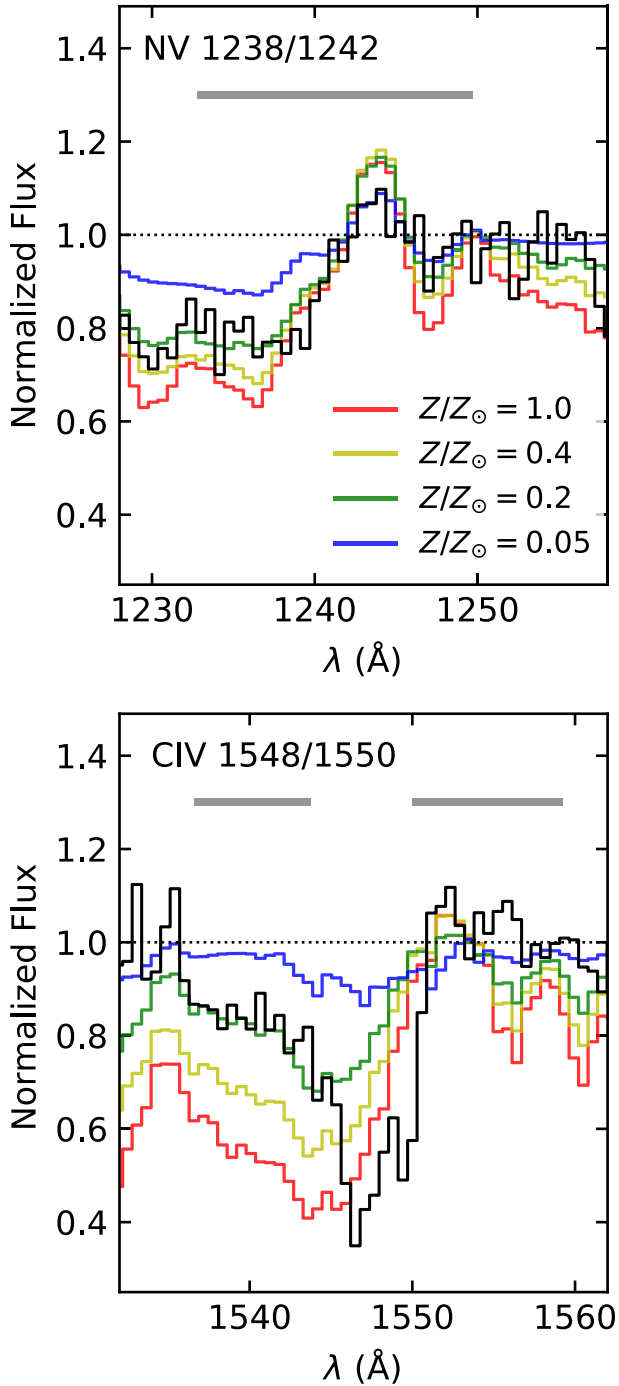
Figure 6. Comparison of the normalized composite spectrum (black) constructed from the GTC individual spectra with STARBURST99 models around the wind lines N v (up) and C iv (down). STARBURST99 models use a stellar population age of 100 Myr and metallicities of 0.05 (blue), 0.2 (green), 0.4 (yellow), and $1.0\,Z_\odot$ (red), as indicated. The spectral windows used to perform the χ^2 minimization are marked in grey. Regions of strong interstellar absorption in C iv were excluded in the fit. Models with metallicity $Z_*/Z_\odot = 0.2$ reproduce quite well the line profiles of the high-ionization N v and C iv lines, in particular the blueshifted absorption of the P-Cygni profile of C iv that is the most metallicity sensitive feature in the UV (Chisholm et al. 2019).

Table 4. χ^2 minimization for stellar models.

LAE	d.o.f. (1)	$Z_*/Z_\odot$ (2)	χ^2 (3)	χ^2/d.o.f. (4)	$\Delta\sigma$ (5)
BG0201+3228	47	0.05	67.12	1.43	1.34
		0.20	54.18	1.15	0.00
		0.40	69.75	1.49	1.61
		1.00	108.43	2.31	5.60
BG0755+3445	54	0.05	85.03	1.58	2.21
		0.20	62.09	1.15	0.00
		0.40	79.73	1.48	1.70
		1.00	126.19	2.33	6.17
BG0918+5104	54	0.05	61.68	1.14	0.37
		0.20	57.79	1.07	0.00
		0.40	99.90	1.85	4.05
		1.00	183.90	3.41	12.14
BG1429+1202	42	0.05	95.36	2.27	4.72
		0.20	57.94	1.38	0.63
		0.40	52.14	1.24	0.00
		1.00	64.96	1.55	1.40
BG1501+3042	44	0.05	70.02	1.87	2.38
		0.20	47.67	1.08	0.00
		0.40	66.39	1.51	2.00
		1.00	119.98	2.73	7.71

Note. (1) Degrees of freedom; (2) metallicity of the synthesis models (assuming $Z_\odot = 0.02$); (3) total χ^2 for each model (equation 7); (4) reduced χ^2; and (5) 1σ deviation between the goodness of fit of each model and the best-fitting model.

continuum and the light contamination from the foreground lens galaxy.

The total χ^2 is computed by comparing all the included spectral elements of our normalized spectra with those from the models with different metallicities:

$$\chi^2 = \sum_i \left(\frac{\text{model}(i) - \text{data}(i)}{\sigma(i)} \right)^2, \qquad (7)$$

where $\sigma(i)$ is the error of the spectral element i. Table 4 shows the values of the metallicities that minimized χ^2 for a given synthesis model. We also show the significance of the difference between the goodness of fit of each model and the best-fitting model, $\Delta\sigma$, calculated for a χ^2 distribution with certain number of degrees of freedom (d.o.f.).

As shown in Table 4, stellar synthesis models with metallicity $Z_*/Z_\odot \simeq 0.2$ are preferred over other solutions in almost all LAEs, with χ^2/d.o.f. ranging from 1.07 to 1.38. We double-check this by generating a high S/N composite spectrum constructed from the five GTC individual spectra. The resulting composite spectrum has higher S/N in the continuum and is less affected by sky-subtracted residuals and spurious features due to intervening absorption systems. Fig. 6 shows the stacked spectrum around the wind lines N v and C iv, as well as the STARBURST99 models with different metallicities. As clearly seen in this figure, models with metallicity $Z_*/Z_\odot \simeq 0.2$ reproduce quite well the line profiles in these regions, in line with the results from our χ^2 minimization.

Note however that for two LAEs, BG0918–5104 and BG1429+1202, other solutions are also accepted with a 1-σ deviation from the best-fitting model below 1 (see Table 4). For BG0918+5104, both models with $Z_*/Z_\odot = 0.05$ and 0.20 provide good fits to the GTC spectrum with χ^2/d.o.f. $= 1.14$ and 1.07, respectively, and a $\Delta\sigma$ between these two models of only 0.37. This

suggests that the metallicity of BG0918+5104 should lie between these two values, being likely the lowest metallicity LAE in our sample, which in turn might explain the strong nebular emission seen in its spectrum (see Fig. 4). On the other hand, the spectrum of BG1429+1202 is better explained by a model with stellar metallicity of $Z_*/Z_\odot \simeq 0.4$. It is worth noting that a slightly large metallicity of $Z_*/Z_\odot \sim 0.6$ was inferred recently by Chisholm et al. (2019) for BG1429+1202. These authors use, however, multiple single age and metallicity models to fit the UV stellar continuum, while we are using continuous star formation models with a fixed age of 100 Myr. Our analysis is therefore limited to discrete models with a set of five metallicities. Consequently, we can only say that a model with stellar metallicity of $Z_*/Z_\odot \simeq 0.4$ is favoured with respected to the other models ($Z_*/Z_\odot = 0.05, 0.20, 1.00$, or 2.00). In addition, the blueshifted absorption of C IV in BG1429+1202 is severely affected by strong sky residuals (at $\lambda_{obs} \sim 5890$–5896 Å), and therefore was not included in the fit. As already shown in several works (e.g. Quider et al. 2009, 2010; James et al. 2014; Marques-Chaves et al. 2018, but in particular in Chisholm et al. 2019), the spectral region encompassing the blueshifted P-Cygni absorption is the most metallicity sensitive feature in the UV.

5.4 Lyα line

Our spectra show prominent and narrow Lyα emission lines (see Fig. 5). We measure Lyα fluxes ranging from (3.0–11.5) × 10^{-16} erg s^{-1} cm^{-2}, much higher (by factors of 1.4–4.7) than the ones measured within the 1 arcsec-radius BOSS fibres (Shu et al. 2016b), as a consequence of the large image separation in these LAEs. By determining the stellar continuum on both sides of the Lyα line, we measure Lyα rest-frame equivalent widths $EW_0 \simeq$ 16–50 Å. The Lyα EW_0 of BG0918+5104 and BG1501+3042 are smaller than the lower limit $EW_0 > 20$ Å commonly adopted to define them as LAEs. In all LAEs the Lyα line is spectrally resolved with FWHM ranging between $\simeq$230 and 400 km s^{-1}, by fitting a Gaussian and correcting it for the instrumental broadening. All quantities are summarized in Table 2.

All LAEs show asymmetric Lyα line profiles (see Fig. 5). At our spectral resolution and depth we do not detect any clear blueshifted component emission in any LAE. For three LAEs (BG0742+3341, BG0755+3445, and BG1429+1202), however, the Lyα line has its maximum intensity very close to, or even consistent with the systemic velocity (see Section 5.1). These are the ones that show narrower Lyα profiles (230–330 km s^{-1} FWHM) suggestive of less scatter from low H I column densities and/or that Lyα photons freely escape through a clumpy ISM (e.g. Zheng & Wallace 2014; Verhamme et al. 2015, 2018; Claeyssens et al. 2019). On the other hand, in addition to the prominent Lyα emission line, BG0201+3228 shows also an underlying broad Lyα absorption (see Fig. 2). This may indicate that the neutral gas in this LAE is inhomogeneous with both high and low column density H I regions (see Jaskot et al. 2019; McKinney et al. 2019), in line with the large covering fraction measured in Section 5.2 [C_f (H I) $\simeq 0.96$].

Our GTC spectra are subject to variable slit-losses, since the observations were carried out through narrow slits (1.0 and 1.2 arcsec wide) covering only a fraction of the total flux of these LAEs. In order to put our spectra on an absolute flux scale, we use the PYTHON package PYPHOT 1.0.1[4] to compute synthetic photometry of the GTC extracted spectra and compare to the total photometry

[4]http://mfouesneau.github.io/docs/pyphot/

derived in Section 4.1 and listed in Table 2. The comparison is done using the *g* band ($\lambda_{min} \simeq 4000$ Å, $\lambda_{max} \simeq 5350$ Å) to avoid the contamination in the LAEs spectra of the stellar light redward the rest-frame 4000 Å break of the foreground lens, which is redshifted to the optical *i* band in all LAE spectra. Depending on each LAE, we find correction factors to account for slit-losses ranging between 0.35 and 0.90.

Having the GTC spectra on an absolute flux scale, we derive the intrinsic Lyα luminosity of these LAEs by using the following formula:

$$L_{\mathrm{Ly}\alpha} = 4\pi D_\mathrm{L}^2 F_{\mathrm{Ly}\alpha}^{\mathrm{obs}} \times \frac{1}{\mu} \times \frac{1}{f}, \qquad (8)$$

where $L_{\mathrm{Ly}\alpha}$ is given in units of erg s^{-1}, D_L in cm, and *f* is the correction factor to account for slit-losses.

Assuming case-B recombination and the Kennicutt (1998) conversion, the Lyα luminosity can be translated into a star formation rate:

$$\mathrm{SFR}\,(\mathrm{Ly}\alpha) = 9.1 \times 10^{-43} L_{\mathrm{Ly}\alpha} \times 10^{0.4 \times A_{\mathrm{Ly}\alpha}} \times \frac{1}{1.8}, \qquad (9)$$

assuming the Chabrier (2003) IMF, where $A_{\mathrm{Ly}\alpha} = 10.2 \times E(B - V)$ is the attenuation at 1215 Å (Reddy et al. 2016a). The nebular colour excess is assumed to be the same as the one measured for the stellar continuum (e.g. Erb et al. 2006; Puglisi et al. 2016).

Comparing the measurements of SFRs from the rest-frame UV (Section 4.3) and Lyα, we find Lyα escape fractions, defined as $f_{\mathrm{esc}}\,(\mathrm{Ly}\alpha) = \mathrm{SFR}_{\mathrm{Ly}\alpha}/\mathrm{SFR}_{\mathrm{UV}}$, between 0.11 and 0.37 (summarized in Table 2).

Note, however, that our spectroscopic measurements of EW_0 (Lyα) and f_{esc} (Lyα) are likely underestimated, at least compared to those measured from narrow-band imaging surveys. Star-forming galaxies, such as LAEs or LBGs, show Lyα emission more spatially extended than the rest-frame UV continuum (e.g. Steidel et al. 2011; Momose et al. 2014; Matthee et al. 2016; Wisotzki et al. 2016; Leclercq et al. 2017), and in some cases with its emission spatially offset from the peak of their UV continuum (e.g. Shibuya et al. 2014a; Matthee et al. 2016; Erb et al. 2019; Hoag et al. 2019). As a result, it has been shown that photometric measurements of EW_0 (Lyα) are on average $\sim$5 times larger than those derived using long-slit spectra (see Steidel et al. 2011; Erb et al. 2014).

This effect should be even more prominent in gravitational lensed systems, like the BELLS GALLERY LAEs. To investigate this, the spatial profiles of Lyα and UV continua of these LAEs were extracted along the slit direction by summing the spectra in specific wavelength ranges along the dispersion direction: $\approx$1210–1224 Å rest frame for the Lyα line, and several tens Angstroms redward and blueward of Lyα for the UV continuum. Both Lyα and UV continuum profiles are then normalized to their maximum. Fig. 7 shows normalized spatial profiles of the UV continuum and Lyα line. For three lensed LAEs, BG0201+3228, BG1429+1202, and BG1501+3042, we find clear differences between the Lyα and UV continuum 1D spatial profiles. The Lyα emission in the lensed LAEs BG0201+3228 and BG1501+3042 presents a more extended profile than the UV continuum, while for BG1429+1202 the Lyα emission appears brighter in the inner region between the lensed images A and B than its UV continuum (similar results found in Marques-Chaves et al. 2017). It is worth noting that the Lyα and UV continuum emission of the lensed images B and C in BG0755+3445 show different Lyα to UV continuum ratios compared with the lensed images A and D, resulting in different EW_0 (Lyα). Finally, the
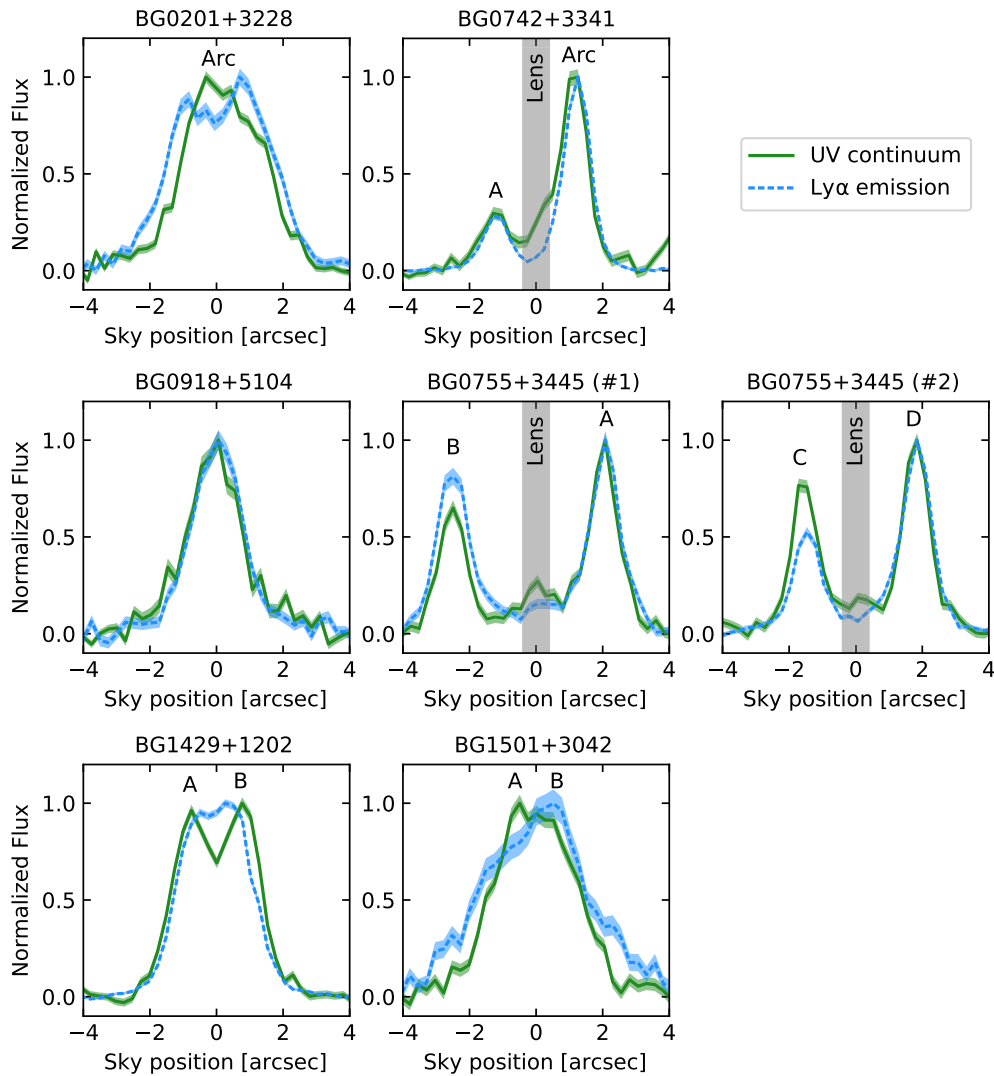
Figure 7. Normalized spatial profiles along the slit of the rest-frame UV continuum (green) and Lyα emission (blue). Shaded regions show the $\pm 1\sigma$ errors of the spatial profiles. For the LAEs BG0201+3228, BG1429+1202 and BG1501+3042 the peak of the Lyα emission is spatially offset with respect to the peak of the UV continuum. The lensed images B and C of BG0755+3445 show different Lyα to UV continuum ratios compared with the lensed images A and D, resulting in different EW_0 (Lyα).

spatial distribution of Lyα in BG0742+3341 and BG0918+5104 appears to follow the UV continuum, although we stress that the orientation of the long slit in BG0742+3341 is not ideal to look for extended Lyα emission, since it was placed perpendicular to the extended arc.

Overall, our results are insufficient for definitive conclusions on the intrinsic morphology and extension of Lyα. However, the differences between the 1D spatial profiles of Lyα and UV seen in Fig. 7 already suggests intrinsic differences on the morphology and/or spatial offsets between Lyα and UV emission. As a result, one should expect that the Lyα emission measured in the spectra is subject to larger slit-losses than the UV continuum, since the GTC long slits were centred on the brightest UV lensed images of each LAE without any information on the light distribution of the Lyα emission, Different morphologies and/or spatial offsets in the source plane can also lead to differential lensing magnification between the UV and Lyα emission. As Lyα emission is found to be statistically more extended than the UV continuum in star-

forming galaxies, the total magnification of the Lyα emission in our LAEs is likely to be lower than that of the more compact UV continuum.

Integral field spectroscopy or narrow-band imaging observations of the Lyα emission are required to better constrain the intrinsic properties of Lyα (e.g. morphology, luminosity, escape fraction, and rest-frame equivalent width) and investigate possible differential magnification between the Lyα and UV emission.

5.5 Other nebular lines

In addition to the Lyα line, we also detect other nebular emission lines, such as O III] and C III]. Prominent emission in these lines are found predominantly in BG0755+3445 and BG0918+5104 and are detected with high significance (see Fig. 4), whereas for the remaining LAEs these lines are only barely detected (even at $<3\sigma$) or fall in regions of strong night sky lines. Despite this, we provide measurements and upper limits of their fluxes and equivalent widths.

Table 5. Nebular emission lines.

Line	$\lambda_{\rm rest}$ (1)	EW_0 (2)	Flux (3)	Luminosity (4)
		BG0201+3228		
He II	1640.42	<0.10	<1.61	<0.25
[O III]	1660.81	0.08 ± 0.06	0.45 ± 0.32	0.07 ± 0.05
O III]	1666.15	0.19 ± 0.11	0.56 ± 0.32	0.09 ± 0.05
[C III]	1906.68	0.28 ± 0.20	1.23 ± 0.72	0.19 ± 0.11
C III]	1908.68	0.30 ± 0.15	1.34 ± 0.54	0.21 ± 0.09
		BG0755+3445		
He II	1640.42	<0.31	<1.27	<0.16
[O III]	1660.81	<0.30	<1.10	<0.14
O III]	1666.15	0.33 ± 0.25	0.25 ± 0.19	0.03 ± 0.02
[C III]	1906.68	1.23 ± 0.30	1.04 ± 0.25	0.13 ± 0.03
C III]	1908.68	1.10 ± 0.28	0.92 ± 0.23	0.12 ± 0.03
		BG0918+5104		
He II	1640.42	<5.01	<8.36	<0.99
[O III]	1660.81	0.36 ± 0.16	0.56 ± 0.23	0.07 ± 0.03
O III]	1666.15	0.84 ± 0.16	1.29 ± 0.24	0.15 ± 0.03
[C III]	1906.68	–	–	–
C III]	1908.68	1.51 ± 0.21	2.51 ± 0.33	0.30 ± 0.04
		BG1429+1202		
He II	1640.42	<0.48	<1.92	<1.34
[O III]	1660.81	<0.30	<1.21	<0.84
O III]	1666.15	0.17 ± 0.12	0.66 ± 0.47	0.46 ± 0.33
[C III]	1906.68	0.83 ± 0.40[a]	2.39 ± 1.13[a]	1.67 ± 0.79[a]
C III]	1908.68	0.83 ± 0.40[a]	2.39 ± 1.13[a]	1.67 ± 0.79[a]
		BG1502+3042		
He II	1640.42	<1.55	<2.41	<2.19
[O III]	1660.81	<1.55	<2.41	<2.19
O III]	1666.15	<1.55	<2.41	<2.19
[C III]	1906.68	0.46 ± 0.24[a]	0.67 ± 0.35[a]	0.61 ± 0.32[a]
C III]	1908.68	0.46 ± 0.24[a]	0.67 ± 0.35[a]	0.61 ± 0.32[a]

Note. (1) Vacuum wavelength in the rest frame; (2) rest-frame equivalent width; (3) observed flux in units of 10^{-17} erg s^{-1} cm^{-2}. For non-detections upper limits refer to 3σ; (4) intrinsic luminosity (corrected for magnification and slit-losses) in units of $10^8 \times L_\odot$ (where $L_\odot = 3.826 \times 10^{33}$ erg s^{-1}). [a]Refer to the measurements of the C III] 1906,1908 Å doublet using a single Gaussian profile.

These measurements will be useful to gain insight on the nature of the ionizing radiation field of our LAEs and will be investigated further in detail in Section 6.3.

We fit symmetric Gaussian profiles to measure the flux and equivalent width of these lines. For C III] we use two Gaussian profiles to fit simultaneously the C III] 1906,1908 Å doublet, except for BG1429+1202 and BG1501+3042 where we use a single profile due to the low S/N. All nebular lines appear spectrally unresolved at our resolution, so that their profiles have FWHM < 200 km s^{-1} (FWHM < 450 km s^{-1} for BG1501+3042). For non-detections, we provide 3σ upper limits, assuming spectrally unresolved profiles. Some examples of the fitting are shown in Fig. 4 (blue dashed lines).

These measurements are listed in Table 5. We also provide measurements or limits (3σ) of the intrinsic luminosities of these lines, i.e. corrected for magnification and slit-losses, that can be useful for future investigation of the physical properties of the ionized gas.

6 DISCUSSION

6.1 The origin of large EW_0 (Lyα) and $f_{\rm esc}$ (Lyα)

Our sample selection consisted of the follow-up of UV-bright BELLS GALLERY lensed galaxies in order to achieve high S/N continuum spectra. Despite this, these galaxies show prominent Lyα emission lines with EW_0 up to $\simeq 50$ Å, even noting that these measurements are likely underestimated (see Section 5.4). We will now compare other properties of the BELLS GALLERY LAEs to those from other Lyα- and UV-selected galaxies.

In the top left panel of Fig. 8, we show the relation between the rest-frame equivalent widths of the averaged low-ionization ISM lines (using the Si II 1260 Å, C II 1334 Å, and Si II 1526 Å absorption lines) and the Lyα emission of our LAEs. We also add to this plot the measurements of EW_0's of low-ionization ISM lines and Lyα of other $z = 2$–4 LAEs and LBGs (Shapley et al. 2003; Shibuya et al. 2014b; Trainor et al. 2015; Du et al. 2018), as well as other nearby high-redshift analogues (Green Pea galaxies; Henry et al. 2015).

Our measurements confirm previous findings that weaker (i.e. lower EW_0) low-ionization ISM absorption lines are associated with stronger Lyα emission (e.g. Shapley et al. 2003; Shibuya et al. 2014b; Du et al. 2018). Such relation suggests that strong LAEs show, on average, weaker low-ionization ISM absorption lines than typical LBGs due to their lower covering fractions and low column densities that allows Lyα photons to escape more efficiently (e.g. Erb et al. 2010; Jaskot & Oey 2014).

While the covering fraction is known to be sensitive to the spectral resolution, the physical and geometric properties of the ISM can also be investigated through the strength and spectral shape of the observed Lyα line.

Our LAEs show relatively narrow Lyα profiles, with intrinsic (i.e. corrected for the instrumental broadening) FWHMs around 230–400 km s^{-1}, suggestive of a reduced number of scatterings in the ISM with a low H I column density (e.g. Verhamme et al. 2015). We also find small velocity offsets (redshifted) of the Lyα peak relative to the systemic redshifts with a mean value and scatter Δv (Lyα) = 150 ± 90 km s^{-1}. This is similar to the values measured in typical LAEs (Δv (Lyα) $\sim$ 100–300 km s^{-1}, e.g. Finkelstein et al. 2011; Hashimoto et al. 2013; Shibuya et al. 2014b; Hashimoto et al. 2015; Trainor et al. 2015; Amorín et al. 2017; Verhamme et al. 2018), but lower than those found in UV-selected LBGs, by a factor of $\approx$2.7 (Δv (Lyα) $\sim$ 400 km s^{-1}; e.g. Steidel et al. 2010). In particular, BG0742+3341, BG0755+3445, and BG1429+1202 show very small values of Δv (Lyα), around 30–80 km s^{-1}, that are expected for objects with density-bounded H II regions, so that Lyα photons would escape relatively unimpeded from the ionizing sources (e.g. Verhamme et al. 2015).

In Fig. 8 (top right panel), we show the relation between these two quantities derived in our LAEs, Δv (Lyα) and FHWM (Lyα). We compare our results with those found in other high-z LAEs and local analogues. As shown already by Verhamme et al. (2015, 2018), these two quantities are tightly correlated (blue line in Fig. 8) and depend mostly on the H I opacity. This clearly suggests that the BELLS GALLERY LAEs studied here, in particular those showing small values of Δv (Lyα) and FHWM (Lyα), likely present low H I column densities.

This scenario is further supported by the relation between the Lyα escape fraction and EW_0 (Lyα) and Δv (Lyα) shown in the bottom panels of Fig. 8. Our BELLS GALLERY LAEs show Lyα
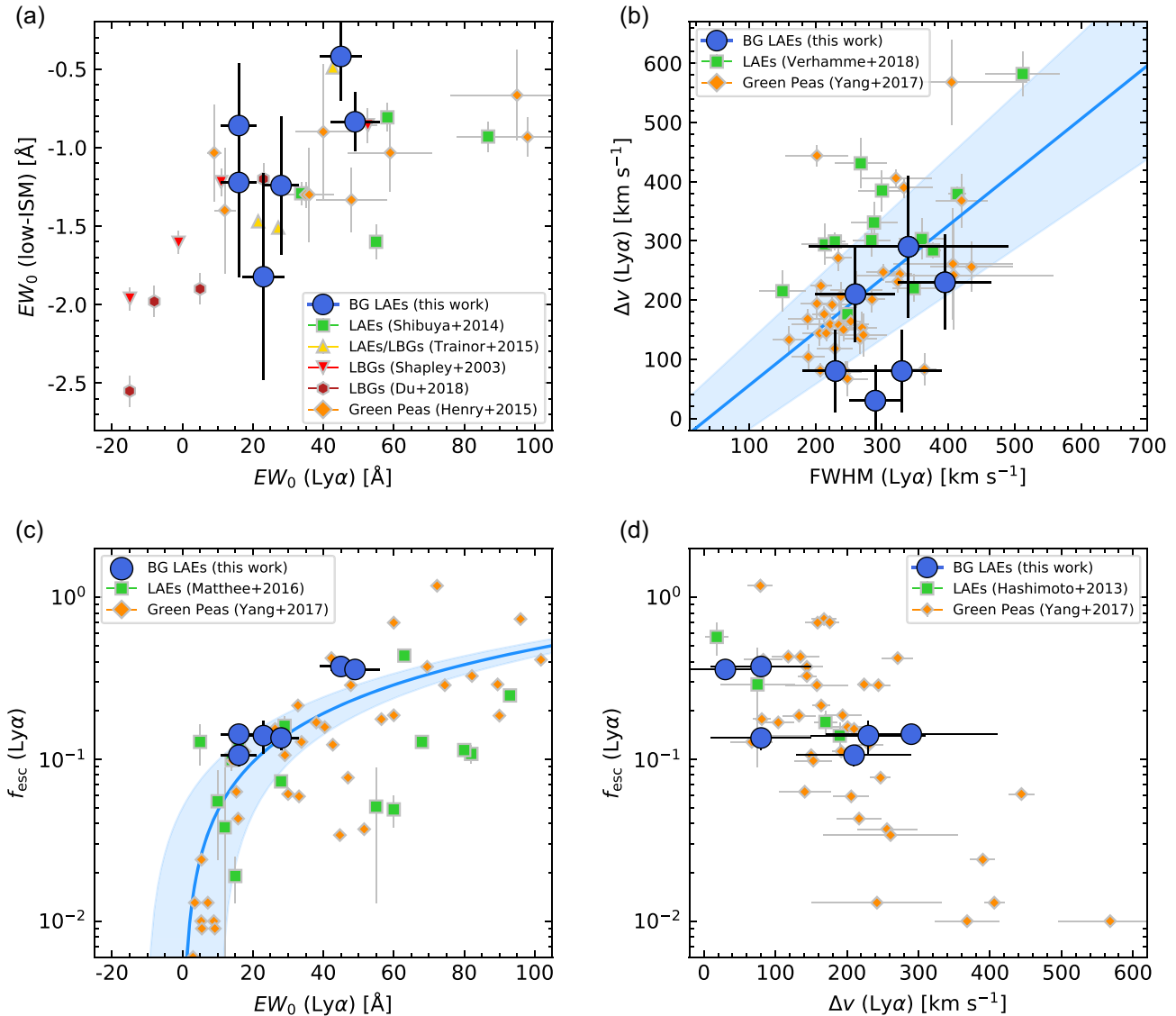
Figure 8. Comparison of several properties of the BELLS GALLERY LAEs (blue circles) to those from other LAEs (Hashimoto et al. 2013; Shibuya et al. 2014b; Trainor et al. 2015; Matthee et al. 2016; Verhamme et al. 2018), LBGs (Shapley et al. 2003; Trainor et al. 2015; Du et al. 2018), and nearby high-redshift analogues (Green Pea galaxies Henry et al. 2015; Yang et al. 2017): (a) rest-frame equivalent width of the averaged low-ionization ISM lines, EW_0(low-ISM), as a function of Lyα equivalent width, EW_0(Lyα); (b) relation between the velocity offset of the Lyα peak relative to the systemic redshift, Δv(Lyα), as a function of the FWHM of the Lyα. These two quantities are correlated (blue line from Verhamme et al. 2018) and depend mostly on the H I opacity; (c) Lyα escape fraction, f_{esc}(Lyα), as a function of EW_0(Lyα). Blue line is the empirical relation derived by Sobral & Matthee (2019); and (d) f_{esc}(Lyα) as a function of Δv(Lyα). In general, large EW_0(Lyα) and f_{esc}(Lyα) are associated with both weak low-ionization ISM absorption lines, narrow Lyα line profiles and small Δv(Lyα).

escape fraction ranging between 0.11 and 0.37 (see Table 2), with a mean value and scatter f_{esc}(Lyα) = 0.21 ± 0.11, in between the range of values found for $z = 2$–4 UV-selected galaxies (f_{esc}(Lyα) ≈ 0.05; e.g. Kornei et al. 2010; Cassata et al. 2015) and other strong Lyα emitters (f_{esc}(Lyα) ≈ 0.30; e.g. Nakajima et al. 2012; Hashimoto et al. 2013; Wardlow et al. 2014; Trainor et al. 2015; Matthee et al. 2016). We recover previous findings that large Lyα escape fraction is associated with small Δv(Lyα) (Hashimoto et al. 2013; Verhamme et al. 2015; Yang et al. 2017; Verhamme et al. 2018) and strong EW_0's (Lyα) (e.g. Trainor et al. 2015; Matthee et al. 2016; Sobral et al. 2017; Yang et al. 2017; Izotov et al. 2020; McKinney et al. 2019), in line with the empirical relation derived by Sobral & Matthee (2019).

Altogether, our findings support the idea that the Lyα emissivity and escape fraction are anticorrelated with the strength of the ISM absorption lines, and the broadness and the velocity offset of the Lyα line. As an example, the two stronger LAEs in our sample, BG0742+3341 and BG1429+1202, those with larger Lyα EW_0's ($\simeq$ 45–49 Å) and escape fractions ($\simeq$ 0.36–0.37), are the ones that show weaker low-ionization ISM absorption ($EW_0 \lesssim 1$ Å), narrower Lyα lines (FWHM $\simeq$ 250–300 km s^{-1}) and smaller Lyα velocity offsets ($\simeq$30–80 km s^{-1}).

Overall, based on the properties of the Lyα line, such as the equivalent width (even noting that is likely underestimated), FWHM, Δv(Lyα), and escape fraction, as well as weak low-ionization ISM absorption lines, the BELLS GALLERY sources

can be classified as LAEs, similar to those found in narrow-band imaging surveys. In addition, our galaxies show steep rest-frame UV slopes ($\overline{\beta_{\mathrm{UV}}} = -1.7 \pm 0.2$), suggesting low dust content, and stellar metallicities of $Z_*/Z_\odot \simeq 0.2$ (see Section 5.3) similar to those inferred in other LAEs (e.g. Ono et al. 2010a; Finkelstein et al. 2011; Nakajima et al. 2013; Kojima et al. 2017), but slightly lower than in the more evolved LBG population ($\gtrsim 0.4 Z_\odot$, e.g. Shapley et al. 2004; Quider et al. 2009, 2010; Sommariva et al. 2012; Marques-Chaves et al. 2018; Chisholm et al. 2019). We note that the remaining BELLS GALLERY LAEs not observed with the GTC are likely to be even more extreme [larger EW_0's (Lyα)] as they have fainter intrinsic UV luminosities (Shu et al. 2016c), yet they show statistically larger observed Lyα fluxes within the 1 arcsec-radius BOSS fibres (see table 1 in Shu et al. 2016b).

6.2 AGN contribution to the UV and Lyα luminosities

In this section we investigate the possible contribution of an active galactic nucleus (AGN) to the UV and Lyα luminosities of our LAEs.

Starting with the UV continuum, the high S/N spectra of these LAEs exhibit both photospheric absorption lines and stellar wind features in the form of P-Cygni profiles (yellow and red lines in Fig. 3, respectively), clearly indicating that the UV luminosity is dominated by stellar emission rather than an AGN. Photospheric absorption lines are formed in the photospheres of young stars and are typically very faint ($EW_0 < 1$ Å; e.g. Prinja 1990). Because of their faintness, the detection of these stellar features requires high S/N continuum spectra, such as those recorded in other highly magnified galaxies (e.g. Pettini et al. 2000; Dessauges-Zavadsky et al. 2010; Quider et al. 2010; Marques-Chaves et al. 2018), in composite spectra (e.g. Shapley et al. 2003; Du et al. 2018) or in very deep spectroscopic observations of individual non-lensed sources (>20h exposure time, e.g. Marchi et al. 2019). The strength of some of these features (e.g. Si III 1417 Å, C III 1426 Å, S V 1501 Å) are also known to be related with the stellar metallicity, such as they appear even weaker at lower stellar metallicities (e.g. Leitherer et al. 2001; Rix et al. 2004; Sommariva et al. 2012) like our LAEs ($Z/Z_\odot \simeq 0.2$, see Section 5.3). For that reason, we would not detect these stellar features if an AGNs were present and its contribution to the UV continuum emission was significant (e.g. type I AGN). These LAEs also show narrow nebular lines (<200 km s^{-1} FWHM), including the Lyα resonant line ($\simeq$ 230–400 km s^{-1}) that is subject of scattering by neutral hydrogen. Furthermore, the lens modelling of these LAEs show that all of them present resolved structures (see Shu et al. 2016c; Marques-Chaves et al. 2017; Cornachione et al. 2018, and Section 3), removing most of the evidence for an AGN contribution to the UV luminosity.

On the contribution of a possible obscured AGN component to the Lyα luminosity, we explore the rest-frame UV emission-line diagnostics of Nakajima et al. (2018b) to identify the source of photoionization. These models were constructed covering a wide range of metallicities ($Z/Z_\odot$ from 10^{-4} to 5.0), ionizing parameters (log (U) between -3.5 and -0.5) and electronic densities ($n = 10$–10^5 cm^{-3}). Following Nakajima et al. (2018b), we employ the UV line diagnostics using equivalent widths of the C III] 1906,1908 Å doublet and the line ratios of C III]/He II (equation 2 in their work). Making use of the measurements of C III] and He II listed in Table 5, we find that the nebular emission in almost all LAEs is excited by star formation, rather than an AGN (see Fig. 9). The exception is BG0918+5104, where their measurements of C III] and the He II upper limit are still consistent with the AGN
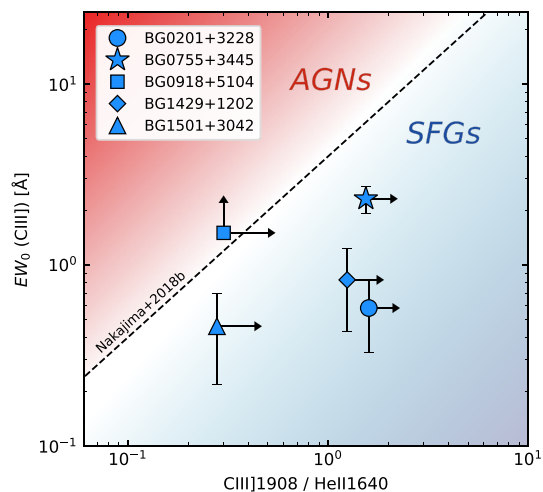

Figure 9. Positions of the BELLS GALLERY LAEs in the diagram of EW_0 (C III]) versus C III]/He II proposed by Nakajima et al. (2018b). This clearly suggests that the gas in these LAEs is excited by star formation and not by an AGN.

photoionization. We note, however, that the [C III] 1906 Å nebular emission in BG0918+5104 is suppressed by the absorption of the Mg II 2796,2803 Å doublet from an intervening absorption system at $z = 1.312$ (see the bottom panel of Fig. 4), and that the spectral region encompassing the He II line is highly affected by the [O I] 5577 Å airglow emission, resulting in a very conservative upper limit of He II (factor of 4–7 larger than those derived in the remaining LAEs).

Therefore, we can conclude that both the UV and Lyα luminosities are due to star formation, rather than an AGN.

6.3 The nature of luminous LAEs

Our LAEs present a wide range of Lyα luminosities, from (1–31) $\times$ 10^{42} erg s^{-1}, which correspond to (0.2 $-$ 5.4) $\times L^*_{\mathrm{Ly}\alpha}$, where $L^*_{\mathrm{Ly}\alpha}$ is the Lyα luminosity of typical $z \sim 2.5$ LAEs ($L^*_{\mathrm{Ly}\alpha} = 5.8 \times 10^{42}$ erg s^{-1}; Sobral et al. 2018b). In the UV continuum, the intrinsic absolute magnitudes of the LAEs are found to be in the range of $-20 \geq M_{\mathrm{UV}}$ (AB) ≥ -23. Considering the UV luminosity of typical $z \sim 2.3$ star-forming galaxies as $M^*_{\mathrm{UV}} = -20.70$ (Reddy & Steidel 2009), these LAEs span the UV luminosity range from $0.5 \times L^*_{\mathrm{UV}}$ to $10 \times L^*_{\mathrm{UV}}$.

In Fig. 10(a), we show the Lyα luminosities and rest-frame UV absolute magnitudes of the six BELLS GALLERY LAEs studied in this work. These values have been corrected for gravitational lensing and flux losses, and are summarized in Table 2. In general, brighter M_{UV} objects have larger Lyα luminosities, as expected since both values increase with the SFRs.

We also add to Fig. 10 the remaining 13 BELLS GALLERY LAEs imaged with *HST*. To do so, we used the *F*606W magnification-corrected rest-frame UV magnitudes calculated from the best-fitting source model presented in Shu et al. (2016c). Their Lyα luminosities were calculated using the fluxes measured from the 1 arcsec-radius BOSS fibres (see Shu et al. 2016b) after correction for the lensing magnification. We assume again similar lensing magnifications for the Lyα emission and the rest-frame UV continuum. We note, however, that these Lyα luminosities should be regarded as lower limits, since no corrections on the flux-losses from the BOSS fibres were applied. These galaxies present relatively fainter UV
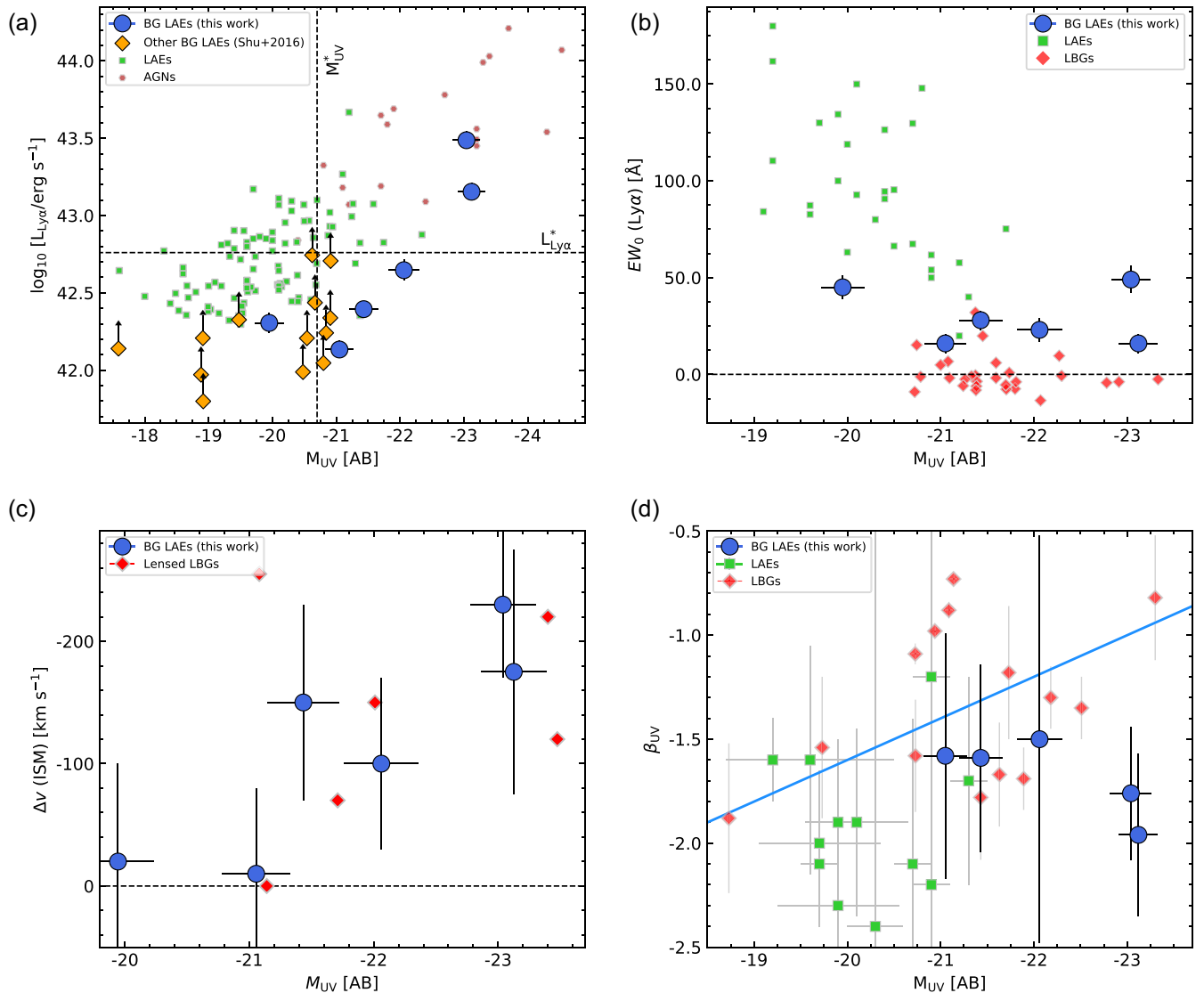
Figure 10. The relationship of rest-frame UV absolute magnitudes of our BELLS GALLERY LAEs (blue circles) on other properties: (a) relation between rest-frame UV and Lyα luminosities. Horizontal and vertical dashed lines mark, respectively, the Lyα luminosity and UV absolute magnitude of typical $z \sim 2.5$ LAEs (Sobral et al. 2018b) and LBGs (Reddy & Steidel 2009). Our LAEs span a wide range of luminosities, both in Lyα (($0.2 - 5.4) \times L^*_{Ly\alpha}$) and UV (($0.5 - 10) \times L^*_{UV}$). The remaining BELLS GALLERY LAEs imaged with *HST* (Shu et al. 2016c) are also shown in orange. Other $z \sim 2$–3 LAEs and AGNs selected from dedicated narrow-band surveys with spectroscopic follow-up (Ouchi et al. 2008; Zheng et al. 2016; Sobral et al. 2018a) are shown in green squares and red circles, respectively. (b) Lyα equivalent widths as a function of M_{UV}. Despite the large UV luminosities, our LAEs show prominent Lyα emission lines with EW_0 up to $\simeq 50$ Å. Green and red symbols mark the measurements of other LAEs (Ouchi et al. 2008; Sobral et al. 2018a) and UV-bright LBGs (Lee et al. 2013); c) relation between the velocity offset of the ISM absorption lines relative the UV absolute magnitude. Red diamonds mark the measurements of other lensed LBGs (Pettini et al. 2000; Quider et al. 2009, 2010; Dessauges-Zavadsky et al. 2010; Patrício et al. 2016; Marques-Chaves et al. 2018). Large outflowing velocities are noticeable for the most luminous LAEs and LBGs. This clearly suggests that the most luminous star-forming galaxies experience strong outflows caused by the large mechanical energy input from supernova explosions and stellar winds; and (d) UV slope (β_{UV}) as a function of the intrinsic absolute magnitudes of our LAEs (blue). Other symbols mark these measurements in other $z = 2$–3 LAEs (green; Sobral et al. 2018a; Santos et al. 2019) and $z = 2$–4 LBGs (orange; Shapley et al. 2003; Bouwens et al. 2009; Lee et al. 2011). Blue line is the $\beta_{UV} - M_{UV}$ relation of Bouwens et al. (2009) for $z \sim 2.5$ LBGs. The luminous LAEs BG1429–1202 and BG1501+3042 ($M_{UV} \sim -23$) show blue UV slopes despite their large luminosities and star formation rates.

luminosities than those from the GTC survey, with UV absolute magnitudes ranging from −17.6 to −21.0 (AB).

In order to put the BELLS GALLERY LAEs into context, we compare their luminosities with other $z \sim 2$–3 LAEs selected from dedicated 1–4 deg² wide narrow-band surveys with spectroscopic follow-up (Ouchi et al. 2008; Zheng et al. 2016; Sobral et al. 2018a). From these surveys, a fraction of LAEs have been found to be powered by AGNs [red symbols in panel (a) of Fig. 10], particularly

in the bright end, by the detection of broad (FWHM > 1000 km s⁻¹) emission lines (e.g. Lyα, C IV, or C III]), or slightly narrow high-ionization lines (such as N V, C IV, and He II) with line ratios typically seen in AGNs (e.g. Hainline et al. 2011).

Overall, our LAEs show statistically lower Lyα luminosities than those selected from narrow-band imaging surveys (except BG1429+1202 and BG1501+3042), yet relatively larger UV absolute magnitudes, likely a consequence of our selection strategy.

The remaining BELLS GALLERY LAEs (in orange in panel a) of Fig. 10) are likely to be more comparable to LAEs selected from narrow-band surveys (both in $L(\text{Ly}\alpha)$ and M_{UV}) if the correction for slit-losses of the Lyα flux within the 1 arcsec-radius BOSS fibres are similar to those of the GTC sample (a factor of $\sim$3–6).

Recently, Sobral et al. (2018a) showed that the fraction of AGN-dominated sources increases strongly with increasing Lyα and UV luminosities, reaching to about 100 per cent for LAEs with luminosities above $2 \times L_{\text{Ly}\alpha}^*$ or L_{UV}^* (i.e. $L_{\text{Ly}\alpha} > 10^{43.3}$ erg s^{-1} or $M_{\text{UV}} < -21.5$ AB). These authors argued that the dust formed in very luminous, purely star-forming galaxies prevents such galaxies being observed in the UV or Lyα if they are more luminous than this limit (see also Konno et al. 2016).

However, as shown in Fig. 10 (panel a), there are several LAEs with luminosities larger than $2 \times L^*$ (in Lyα or UV), including three out of the six BELLS GALLERY LAEs observed with the GTC. Their spectra exhibit both photospheric absorption lines and stellar wind features, clearly indicates that the strong UV continuum and Lyα luminosity are due to star formation, rather than an AGN (see Section 6.2).

Our results demonstrate that LAEs at $z \sim 2$–3 can be as luminous as $L_{\text{Ly}\alpha} \simeq 10^{43.5}$ erg s^{-1} (or $\simeq 5 \times L_{\text{Ly}\alpha}^*$) and $M_{\text{UV}} \simeq -23$ AB (or $\simeq 10 \times L_{\text{UV}}^*$) without invoking an AGN component, in contrast to the previous findings. It is worth noting that, while luminous LAEs at $z \sim 2$–3 appear scarce, as they have not been previously detected in these 1–4 deg^2 wide surveys (Ouchi et al. 2008; Zheng et al. 2016; Sobral et al. 2018a), a few UV-luminous ($M_{\text{UV}} \sim -23$ AB) non-active LBGs at similar redshifts have been already discovered (e.g. Allam et al. 2007; Lee et al. 2013; Le Fèvre et al. 2013; Marques-Chaves et al. 2018). However, UV-luminous LBGs present on average a strongly suppressed Lyα line (see panel b of Fig. 10) consistent with large neutral gas column densities ($N(\text{H\,\textsc{i}}) > 10^{20}$ cm^{-2}, Dessauges-Zavadsky et al. 2010; Marques-Chaves et al. 2018). Moreover, these luminous LBGs also appear more evolved than our luminous LAEs, as they show larger metallicities, stronger ISM absorption lines, and redder slopes suggesting large dust attenuation. Similar luminosities have been also found in very bright $z > 6$ UV- or Lyα-selected star-forming galaxies (e.g. Ouchi et al. 2009; Sobral et al. 2015; Roberts-Borsani et al. 2016; Matthee et al. 2017; Ono et al. 2018; Shibuya et al. 2018; Hashimoto et al. 2019; Matsuoka et al. 2019), although the contribution of a possible AGN needs to be investigated in more detail in future observations with the *James Webb Space Telescope*.

We also investigate the influence of such large luminosities and star formation rates on the kinematics of the gas. In panel (c) of Fig. 10, we compare the velocity offset of the ISM absorption lines relative to the systemic redshift and the absolute magnitudes of our LAEs. We also show these quantities measured in other lensed LBGs with damped Lyα absorption (Pettini et al. 2000; Dessauges-Zavadsky et al. 2010; Quider et al. 2010; Marques-Chaves et al. 2018) or weak emission ($EW_0 < 20$ Å; Quider et al. 2009; Patrício et al. 2016). These LBGs also present similar range of UV absolute magnitudes as our LAEs, from -21 to -23.4 (AB). In this case, both LAEs and LBGs appear to share the same global pattern. Large outflowing velocities of $\Delta v(\text{ISM}) \simeq -200$ km s^{-1} are more noticeable for the most luminous LAEs (BG1429+1202 and BG1501+3042) and LBGs (8 o'clock and HLock01-B galaxies: Dessauges-Zavadsky et al. 2010, Marques-Chaves et al. 2018, respectively). For the less luminous ones, the ISM absorption lines have the minimum intensity very close to the systemic velocities. This highly suggests that the

most luminous star-forming galaxies, the ones that show larger star formation rates, experience strong outflows caused by the mechanical energy input from supernova explosions and stellar winds.

More interestingly, the most luminous LAEs in our sample, BG1429+1202 and BG1501+3042 (with $M_{\text{UV}} \sim -23$), also present bluer β_{UV} slopes than the fainter ones (panel d in Fig. 10), in contrast to the general idea that β_{UV} is much redder at higher luminosities and SFRs (e.g. Bouwens et al. 2009; Lee et al. 2011; Hashimoto et al. 2017; Oyarzún et al. 2017). In addition, other spectral properties of these luminous LAEs are broadly similar to those found in much fainter LAEs: e.g. large $f_{\text{esc}}(\text{Ly}\alpha)$, weak ISM absorption lines and low stellar metallicity; all of them thought to be closely related to an early evolutionary state of a galaxy.

It is possible therefore that these luminous LAEs are experiencing a very recent and massive burst of star formation, so that they have only had time to form small amounts of dust. Recent close-by merger events or accretion of gas may have triggered the large luminosities and SFRs of these galaxies. For example, BG1501+3042 is composed by two UV-bright components separated by only $\simeq 4$ kpc in projection (see Fig. 2), highly suggesting a major merger event. Similarly, the reconstructed source-plane image of BG0201+3228 also reveals three UV-bright components separated by only ~ 1.2 kpc (Shu et al. 2016c; Cornachione et al. 2018). Additionally, the extreme feedback associated with the large SFRs may produce channels through the ISM where Lyα photons could escape more efficiently. A clumpy ISM could explain the relatively weak ISM absorption lines (and neutral gas covering fractions) and the large Lyα escape fractions in these luminous LAEs.

Regardless the mechanisms responsible for the large luminosities (recent episodes of merger, interaction, or accretion of gas), their vigorous SFRs will likely change dramatically their chemical and dust composition in a very short time-scale, converting them in more evolved LBGs. Such a short time-scale could in principle explain the rarity of these UV/Lyα luminous systems.

7 SUMMARY AND CONCLUSIONS

This work presents the results of a GTC and WHT imaging and spectroscopic follow-up of six BELLS GALLERY lensed LAEs. They were chosen to have large image separations and flux densities in optical bands in order to perform high S/N studies of their physical properties. These LAEs, with redshifts between 2.36 and 2.82, are lensed by massive early-type galaxies at $z \simeq 0.39$–0.72 providing total magnifications of $\simeq 3$–18. From the analysis of these data we obtain the following results:

(i) We spectroscopically confirmed the lensing nature of these systems through the detection of emission/absorption spectral features in several lensed images of each LAE. One of these, BG1501+3042 at $z = 2.645$, is a new confirmed lensed LAE with three detected lensed images. This system is composed by a pair interacting/merging galaxies magnified by a factor of $\simeq 3.2$. In addition, we measured the systemic redshifts of all LAEs using nebular emission from H\,\textsc{ii} regions, stellar absorption from the photospheres of massive stars, and fine-structure emission lines.

(ii) These LAEs show similar properties to those selected from narrow-band imaging surveys, even though they have been selected through different methods. We measure Lyα rest-frame equivalent widths ranging from 16 to 50 Å and Lyα escape fractions ranging from 10 per cent to 40 per cent assuming case-B recombination. These measurements are likely underestimated due to larger slit-

losses of the Lyα flux relative to the UV continuum. These LAEs show weaker low-ionization ISM lines when compared to the more evolved LBG population. In addition, we find that for almost all LAEs their N V and C IV stellar P-Cygni profiles are well fitted by STARBURST99 stellar synthesis models with metallicity of $Z/Z_\odot = 0.2$.

(iii) We measure dust-corrected star formation rates up to $\simeq 180\,M_\odot\,\mathrm{yr}^{-1}$, yet these LAEs appear relatively blue ($\beta_{\mathrm{UV}} \simeq -1.5$ to -2.0) showing evidence of little dust attenuation, $E(B-V) = 0.10$–0.20. They present rest-frame UV and Lyα intrinsic luminosities in the range of $-20 < M_{\mathrm{UV}} < -23$ and $L_{\mathrm{Ly}\alpha} = (1$–$30) \times 10^{42}\,\mathrm{erg\,s}^{-1}$, respectively. None of them show any evidence for AGN activity. Even knowing that luminous LAEs ($> 2 \times L^*$) are likely rare, they exist also at $z = 2$–3 and can show luminosities at least up to $L_{\mathrm{Ly}\alpha} \simeq 10^{43.5}\,\mathrm{erg\,s}^{-1}$ and $M_{\mathrm{UV}} \simeq -23$ AB, without invoking to an AGN component, in contrast with previous findings.

(iv) We show that f_{esc} (Lyα) increases with increasing EW_0 (Lyα). We find that LAEs with lower EW_0 (Lyα) and f_{esc} (Lyα) present broader Lyα line profiles with their peak more redshifted relative to their systemic redshifts, by $\simeq 200$–$300\,\mathrm{km\,s}^{-1}$, consistent with Lyα photons being scattered by receding outflowing gas. On the other hand, for LAEs with larger EW_0 (Lyα) and f_{esc} (Lyα), the Lyα line peaks close to (or consistent with) the systemic redshift. The Lyα line in these ones also present narrower profiles, suggestive of less scatter from low H I column densities that favours the escape of Lyα photons.

(v) On the kinematics, the centroids of the ISM absorption lines in some of these LAEs appear blueshifted up to $200\,\mathrm{km\,s}^{-1}$ relative to their systemic redshift, indicative of large galaxy-scale outflows due to radiation pressure of the most massive and luminous stars. These LAEs are the ones that present larger UV and Lyα luminosities, and therefore larger star formation rates. On the other hand, for the less luminous LAEs, the ISM absorption lines have the minimum intensity close to the systemic velocity.

(vi) We identify a trend for EW_0 (Lyα) to increase with decreasing EW_0 (low-ISM). Low-ionization ISM lines show residual intensities of about $I/I_0 \simeq 0.3$–0.7 indicating partial coverage of the interstellar gas. Assuming the optically thick regime and using the low-ionization ISM line Si II 1260 Å, we measure dust-corrected covering fractions of neutral gas C_f (H I) between ~ 0.68–0.96.

Overall, we have shown that LAEs can present a wide range of luminosities and are not restricted to the faint end only, as previously thought. Interestingly, the most luminous ones also present steeper UV slopes. We speculate that these luminous LAEs may be particular cases of very young starburst galaxies that have only had time to form small amounts of dust. If so, this phase should last only a few Myr, as their large SFRs will likely enrich the chemical and dust composition, converting these LAEs in more evolved LBGs. Such a short time-scale could in principle explain the very low number density of these UV and Lyα luminous systems.

REFERENCES

Ahn C. P. et al., 2012, ApJS, 203, 21

Ajiki M. et al., 2003, AJ, 126, 2091

Allam S. S., Tucker D. L., Lin H., Diehl H. T., Annis J., Buckley-Geer E. J., Frieman J. A., 2007, ApJ, 662, L51

Álvarez-Márquez J., Burgarella D., Buat V., Ilbert O., Pérez-González P. G., 2019, A&A, 630, A153

Amorín R. et al., 2017, Nat. Astron., 1, 0052

Benn C., Dee K., Agócs T., 2008, in Proceedings of SPIE, Ground-based and Airborne Instrumentation for Astronomy II. Marseille, France, p. 70146X

Bertin E., 2006, in Gabriel C., Arviset C., Ponz D., Enrique S., eds, ASP Conf. Ser. Vol. 351, Astronomical Data Analysis Software and Systems XV. Astronomical Society of the Pacific, San Francisco, p. 112

Bertin E., 2010, Astrophysics Source Code Library, record ascl:1010.068

Bertin E., Arnouts S., 1996, A&AS, 117, 393

Blanton M. R. et al., 2017, AJ, 154, 28

Bolton A. S., Burles S., Koopmans L. V. E., Treu T., Gavazzi R., Moustakas L. A., Wayth R., Schlegel D. J., 2008, ApJ, 682, 964

Bond N. A., Gawiser E., Gronwall C., Ciardullo R., Altmann M., Schawinski K., 2009, ApJ, 705, 639

Bond N. A., Gawiser E., Guaita L., Padilla N., Gronwall C., Ciardullo R., Lai K., 2012, ApJ, 753, 95

Bouwens R. J. et al., 2009, ApJ, 705, 936

Bouwens R. J. et al., 2015, ApJ, 803, 34

Bouwens R. J. et al., 2016, ApJ, 833, 72

Brownstein J. R. et al., 2012, ApJ, 744, 41

Cabanac R. A., Valls-Gabaud D., Lidman C., 2008, MNRAS, 386, 2065

Calzetti D., Armus L., Bohlin R. C., Kinney A. L., Koornneef J., Storchi-Bergmann T., 2000, ApJ, 533, 682

Cassata P. et al., 2015, A&A, 573, A24

Chabrier G., 2003, ApJ, 586, L133

Chisholm J. et al., 2018, A&A, 616, A30

Chisholm J., Rigby J. R., Bayliss M., Berg D. A., Dahle H., Gladders M., Sharon K., 2019, ApJ, 882, 182

Claeyssens A. et al., 2019, MNRAS, 489, 5022–5029

Cornachione M. A. et al., 2018, ApJ, 853, 148

Dahle H. et al., 2013, ApJ, 773, 146

Dessauges-Zavadsky M., D'Odorico S., Schaerer D., Modigliani A., Tapken C., Vernet J., 2010, A&A, 510, A26

Du X. et al., 2018, ApJ, 860, 75

Erb D. K., Steidel C. C., Shapley A. E., Pettini M., Reddy N. A., Adelberger K. L., 2006, ApJ, 647, 128

Erb D. K., Pettini M., Shapley A. E., Steidel C. C., Law D. R., Reddy N. A., 2010, ApJ, 719, 1168

Erb D. K. et al., 2014, ApJ, 795, 33

Erb D. K., Berg D. A., Auger M. W., Kaplan D. L., Brammer G., Pettini M., 2019, ApJ, 884, 7

Faisst A. L., Capak P. L., Emami N., Tacchella S., Larson K. L., 2019, ApJ, 884, 133

Finkelstein S. L. et al., 2011, ApJ, 729, 140

Finkelstein S. L. et al., 2013, Nature, 502, 524

France K., Nell N., Green J. C., Leitherer C., 2010, ApJ, 722, L80

Gaia Collaboration, 2016, A&A, 595, A2

Gawiser E. et al., 2007, ApJ, 671, 278

Gazagnes S., Chisholm J., Schaerer D., Verhamme A., Rigby J. R., Bayliss M., 2018, A&A, 616, A29

Guaita L. et al., 2011, ApJ, 733, 114

Gwyn S. D. J., 2008, PASP, 120, 212

Hainline K. N., Shapley A. E., Greene J. E., Steidel C. C., 2011, ApJ, 733, 31

Hashimoto T., Ouchi M., Shimasaku K., Ono Y., Nakajima K., Rauch M., Lee J., Okamura S., 2013, ApJ, 765, 70

Hashimoto T. et al., 2015, ApJ, 812, 157

Hashimoto T. et al., 2017, A&A, 608, A10

Hashimoto T. et al., 2018, Nature, 557, 392

Hashimoto T. et al., 2019, PASJ, 71, 71

Henry A., Scarlata C., Martin C. L., Erb D., 2015, ApJ, 809, 19

Hernán-Caballero A. et al., 2017, ApJ, 849, 82

Hoag A. et al., 2019, MNRAS, 488, 706

Izotov Y. I., Schaerer D., Worseck G., Verhamme A., Guseva N. G., Thuan T. X., Orlitova I., Fricke K. J., 2020, MNRAS, 491, 468

James B. L. et al., 2014, MNRAS, 440, 1794

Jaskot A. E., Oey M. S., 2014, ApJ, 791, L19

Jaskot A. E., Dowd T., Oey M. S., Scarlata C., McKinney J., 2019, ApJ, 885, 96

Jones T., Stark D. P., Ellis R. S., 2012, ApJ, 751, 51

Jones T., Stark D. P., Ellis R. S., 2018, ApJ, 863, 191

Jones T. A., Ellis R. S., Schenker M. A., Stark D. P., 2013, ApJ, 779, 52

Kennicutt R. C., Jr, 1998, ARA&A, 36, 189

Kojima T., Ouchi M., Nakajima K., Shibuya T., Harikane Y., Ono Y., 2017, PASJ, 69, 44

Konno A., Ouchi M., Nakajima K., Duval F., Kusakabe H., Ono Y., Shimasaku K., 2016, ApJ, 823, 20

Kornei K. A., Shapley A. E., Erb D. K., Steidel C. C., Reddy N. A., Pettini M., Bogosavljević M., 2010, ApJ, 711, 693

Koyama Y. et al., 2015, MNRAS, 453, 879

Kusakabe H. et al., 2018, PASJ, 70, 4

Laporte N. et al., 2017, ApJ, 837, L21

Le Fèvre O. et al., 2013, A&A, 559, A14

Leclercq F. et al., 2017, A&A, 608, A8

Lee K.-S. et al., 2011, ApJ, 733, 99

Lee K.-S., Dey A., Cooper M. C., Reddy N., Jannuzi B. T., 2013, ApJ, 771, 25

Leitherer C. et al., 1999, ApJS, 123, 3

Leitherer C., Leão J. R. S., Heckman T. M., Lennon D. J., Pettini M., Robert C., 2001, ApJ, 550, 724

Leitherer C., Ortiz Otálvaro P. A., Bresolin F., Kudritzki R.-P., Lo Faro B., Pauldrach A. W. A., Pettini M., Rix S. A., 2010, ApJS, 189, 309

Marchi F. et al., 2019, A&A, 631, A19

Marques-Chaves R. et al., 2017, ApJ, 834, L18

Marques-Chaves R. et al., 2018, ApJ, 854, 151

Matsuoka Y. et al., 2019, ApJ, 883, 183

Matthee J., Sobral D., Oteo I., Best P., Smail I., Röttgering H., Paulino-Afonso A., 2016, MNRAS, 458, 449

Matthee J., Sobral D., Darvish B., Santos S., Mobasher B., Paulino-Afonso A., Röttgering H., Alegre L., 2017, MNRAS, 472, 772

Matthee J., Sobral D., Gronke M., Paulino-Afonso A., Stefanon M., Röttgering H., 2018, A&A, 619, A136

McKinney J. H., Jaskot A. E., Oey M. S., Yun M. S., Dowd T., Lowenthal J. D., 2019, ApJ, 874, 52

Momose R. et al., 2014, MNRAS, 442, 110

Momose R. et al., 2016, MNRAS, 457, 2318

Morton D. C., 1991, ApJS, 77, 119

Nakajima K. et al., 2012, ApJ, 745, 12

Nakajima K., Ouchi M., Shimasaku K., Hashimoto T., Ono Y., Lee J. C., 2013, ApJ, 769, 3

Nakajima K., Fletcher T., Ellis R. S., Robertson B. E., Iwata I., 2018a, MNRAS, 477, 2098

Nakajima K. et al., 2018b, A&A, 612, A94

Newville M., Stensitzki T., Allen D. B., Ingargiola A., 2014, LMFIT: Non-Linear Least-Square Minimization and Curve-Fitting for Python, https://doi.org/10.5281/zenodo.11813

Oguri M. et al., 2008, ApJ, 676, L1

Ono Y. et al., 2010a, MNRAS, 402, 1580

Ono Y., Ouchi M., Shimasaku K., Dunlop J., Farrah D., McLure R., Okamura S., 2010b, ApJ, 724, 1524

Ono Y. et al., 2018, PASJ, 70, S10

Ouchi M. et al., 2005, ApJ, 620, L1

Ouchi M. et al., 2008, ApJS, 176, 301

Ouchi M. et al., 2009, ApJ, 696, 1164

Oyarzún G. A., Blanc G. A., González V., Mateo M., Bailey John I. I., 2017, ApJ, 843, 133

Patrício V. et al., 2016, MNRAS, 456, 4191

Paulino-Afonso A. et al., 2018, MNRAS, 476, 5479

Peng C. Y., Ho L. C., Impey C. D., Rix H.-W., 2002, AJ, 124, 266

Peng C. Y., Ho L. C., Impey C. D., Rix H.-W., 2010, AJ, 139, 2097

Pettini M., Steidel C. C., Adelberger K. L., Dickinson M., Giavalisco M., 2000, ApJ, 528, 96

Pettini M., Rix S. A., Steidel C. C., Adelberger K. L., Hunt M. P., Shapley A. E., 2002, ApJ, 569, 742

Prinja R. K., 1990, MNRAS, 246, 392

Puglisi A. et al., 2016, A&A, 586, A83

Quider A. M., Pettini M., Shapley A. E., Steidel C. C., 2009, MNRAS, 398, 1263

Quider A. M., Shapley A. E., Pettini M., Steidel C. C., Stark D. P., 2010, MNRAS, 402, 1467

Reddy N. A., Steidel C. C., 2009, ApJ, 692, 778

Reddy N. A. et al., 2015, ApJ, 806, 259

Reddy N. A., Steidel C. C., Pettini M., Bogosavljević M., 2016a, ApJ, 828, 107

Reddy N. A., Steidel C. C., Pettini M., Bogosavljević M., Shapley A. E., 2016b, ApJ, 828, 108

Reddy N. A. et al., 2018, ApJ, 853, 56

Rigby J. R. et al., 2018a, AJ, 155, 104

Rigby J. R. et al., 2018b, ApJ, 853, 87

Ritondale E., Auger M. W., Vegetti S., McKean J. P., 2019, MNRAS, 482, 4744

Rix S. A., Pettini M., Leitherer C., Bresolin F., Kudritzki R.-P., Steidel C. C., 2004, ApJ, 615, 98

Roberts-Borsani G. W. et al., 2016, ApJ, 823, 143

Salpeter E. E., 1955, ApJ, 121, 161

Santos S. et al., 2019, preprint (arXiv:1910.02959)

Savage B. D., Sembach K. R., 1991, ApJ, 379, 245

Schaerer D., de Barros S., Stark D. P., 2011, A&A, 536, A72

Schlafly E. F., Finkbeiner D. P., 2011, ApJ, 737, 103

Shapley A. E., Steidel C. C., Pettini M., Adelberger K. L., 2003, ApJ, 588, 65

Shapley A. E., Erb D. K., Pettini M., Steidel C. C., Adelberger K. L., 2004, ApJ, 612, 108

Shibuya T., Ouchi M., Nakajima K., Yuma S., Hashimoto T., Shimasaku K., Mori M., Umemura M., 2014a, ApJ, 785, 64

Shibuya T. et al., 2014b, ApJ, 788, 74

Shibuya T. et al., 2018, PASJ, 70, S15

Shibuya T., Ouchi M., Harikane Y., Nakajima K., 2019, ApJ, 871, 164

Shu Y. et al., 2015, ApJ, 803, 71

Shu Y., Bolton A. S., Moustakas L. A., Stern D., Dey A., Brownstein J. R., Burles S., Spinrad H., 2016a, ApJ, 820, 43

Shu Y. et al., 2016b, ApJ, 824, 86

Shu Y. et al., 2016c, ApJ, 833, 264

Shu Y., Marques-Chaves R., Evans N. W., Pérez-Fournon I., 2018, MNRAS, 481, L136

Sobral D., Matthee J., 2019, A&A, 623, A157

Sobral D., Matthee J., Darvish B., Schaerer D., Mobasher B., Röttgering H. J. A., Santos S., Hemmati S., 2015, ApJ, 808, 139

Sobral D. et al., 2017, MNRAS, 466, 1242

Sobral D., et al., 2018a, MNRAS, 477, 2817

Sobral D., Santos S., Matthee J., Paulino-Afonso A., Ribeiro B., Calhau J., Khostovan A. A., 2018b, MNRAS, 476, 4725

Sommariva V., Mannucci F., Cresci G., Maiolino R., Marconi A., Nagao T., Baroni A., Grazian A., 2012, A&A, 539, A136

Steidel C. C., Erb D. K., Shapley A. E., Pettini M., Reddy N., Bogosavljević M., Rudie G. C., Rakic O., 2010, ApJ, 717, 289

Steidel C. C., Bogosavljević M., Shapley A. E., Kollmeier J. A., Reddy N. A., Erb D. K., Pettini M., 2011, ApJ, 736, 160

Steidel C. C., Strom A. L., Pettini M., Rudie G. C., Reddy N. A., Trainor R. F., 2016, ApJ, 826, 159

Taniguchi Y. et al., 2009, ApJ, 701, 915

Trainor R. F., Steidel C. C., Strom A. L., Rudie G. C., 2015, ApJ, 809, 89

Verhamme A., Schaerer D., Atek H., Tapken C., 2008, A&A, 491, 89

Verhamme A., Orlitová I., Schaerer D., Hayes M., 2015, A&A, 578, A7

Verhamme A. et al., 2018, MNRAS, 478, L60

Wardlow J. L. et al., 2014, ApJ, 787, 9

Weiner B. J. et al., 2009, ApJ, 692, 187

Wisotzki L. et al., 2016, A&A, 587, A98

Yang H. et al., 2017, ApJ, 844, 171

Zheng Z., Wallace J., 2014, ApJ, 794, 116

Zheng Z.-Y., Malhotra S., Rhoads J. E., Finkelstein S. L., Wang J.-X., Jiang C.-Y., Cai Z., 2016, ApJS, 226, 23

Zitrin A. et al., 2015, ApJ, 810, L12

APPENDIX A: LOWER Z INTERVENING METAL-LINE SYSTEMS

In addition to the absorption lines associated with the ISM gas and stars of each lensed LAE, we also detect other absorption lines from intervening metal systems at lower redshifts. In total we find five intervening metal systems at redshifts between 1.31 and

Table A1. Intervening metal-absorption line systems.

$\lambda_{\rm obs}$ (Å)	Line	$z_{\rm abs}$	EW_0 (Å)
BG0201+3228 − System 1: $z_{\rm abs} = 2.705$			
5164.45	Si IV 1393.75	2.7055	0.47
5197.65	Si IV 1402.77	2.7050	0.45
5734.79[a]	C IV 1548.19	2.7042[a]	0.38[a]
5734.79[a]	C IV 1550.77	2.7040[a]	0.57[a]
6872.02[b]	Al III 1854.71	2.7052[b]	0.89[b]
6900.53	Al III 1862.79	2.7044	0.94
BG0918+5104 − System 1: $z_{\rm abs} = 1.3121$			
5419.80	Fe II 2344.21	1.3120	0.47
5490.11	Fe II 2374.46	1.3121	0.09
5508.68	Fe II 2382.76	1.3119	0.72
6011.78	Fe II 2600.17	1.3121	0.65
6465.10	Mg II 2796.35	1.3120	0.86
6482.65[c]	Mg II 2803.53	1.3123[c]	0.29[c]
BG1429+1202 − System 1: $z_{\rm abs} = 2.1804$			
4855.53	Si II 1526.70	2.1804	0.75
4923.25	C IV 1548.19	2.1800	0.75
4931.90	C IV 1550.77	2.1803	0.38
5115.58	Fe II 1608.45	2.1804	0.49
5313.99	Al II 1670.78	2.1805	0.88
7455.35	Fe II 2344.21	2.1803	0.70
7551.81	Fe II 2374.46	2.1804	0.50
7578.35	Fe II 2382.76	2.1805	1.04
BG1429+1202 − System 2: $z_{\rm abs} = 2.3472$			
5182.16	C IV 1548.19	2.3472	1.37
5190.61	C IV 1550.70	2.3473	0.92
BG1502+3042 − System 1: $z_{\rm abs} = 2.269$			
4556.67	Si IV 1393.75	2.2694	1.67
4584.17[d]	Si IV 1402.77	2.2680[d]	1.22[d]
5064.80[e]	C IV 1548.19	2.2687[e]	1.84[e]
5064.80[e]	C IV 1550.70	2.2687[e]	1.84[e]

[a]Blended with the stellar photospheric absorption S V λ1501 of BG0201+3228.
[b]This intervening absorption line falls in the region of a telluric absorption line (*B* band).
[c]Blended with the nebular emission C III] λ1906 of BG0918+5104.
[d]Blended with the absorption from Si II λ1260 of BG1502+3042.
[e]The measured values refer to the C IV λ1548,1550 doublet given the low spectral resolution of the GTC R1000B grism.

2.70. None of these systems is associated with the LAEs or their corresponding lens, but originates in intervening systems along the line of sight to the LAEs. Table A1 lists the identified intervening metal-absorption lines for each lensed LAE with their redshifts and rest-frame equivalent widths.

This paper has been typeset from a TEX/LATEX file prepared by the author.